

Synthesis and Properties of Fused-Ring-Expanded Porphyrins that were Core-Modified with Group 16 Heteroatoms

Hai-Jun Xu,^[a] John Mack,^[b, d] Di Wu,^[a] Zhao-Li Xue,^[a] Ana B. Descalzo,^[c, e]
Knut Rurack,^{*, [c]} Nagao Kobayashi,^{*, [b]} and Zhen Shen^{*, [a]}

Dedicated to Professor Noboru Ono on the occasion of his 70th birthday

Abstract: The synthesis of a series of novel core-modified and fused-ring-expanded tetraphenylporphyrins is reported. Theoretical calculations and magnetic circular dichroism (MCD) and fluorescence spectroscopic measurements were used to analyze the effect of core modification with Group 16 oxygen, sulfur, selenium, and tellurium atoms on the optical properties and electronic structures of the

porphyrins. Marked redshifts of the Q and B bands and accelerated intersystem-crossing rates were observed, thus making these compounds potentially suitable for use in a variety of applica-

Keywords: density functional calculations • fluorescence • MCD spectroscopy • porphyrinoids • ring expansion

tions. The scope for further fine-tuning of these optical properties based on additional structural modifications, such as the incorporation of fused benzene rings to form ABAB structures by using a thiophene precursor with a fused bicyclo[2.2.2]octadiene ring and the introduction of various substituents onto the *meso*-phenyl rings, is also examined.

Introduction

Porphyrins have long been the focus of intense research interest due to the key role that porphyrinoid π -systems play in various biological processes, such as photosynthesis and respiration. In recent years, research has focused, to a significant extent, on the use of porphyrinoids as opto-electronic materials. Structurally modified porphyrins with strong absorption bands at the red end of the visible-light region and in the 700–1000 nm portion of the near-infrared (NIR) spectrum have been investigated extensively, due to their potential future use in photodynamic therapy^[1–3] and in key material-science applications, such as fluorescent probes,^[4] solar-energy conversion,^[5] nonlinear optical materials,^[6] and NIR dyes.^[5, 7–9] In the future, there is likely to be a growing focus on porphyrinoids that absorb and fluoresce significantly in the second and third telecom windows (1260–1675 nm). Various strategies, such as peripheral fused-ring-expansion,^[10] the introduction of *meso*-alkynyl substituents,^[11, 12] and the formation of porphyrin oligomers,^[13] have been adopted to redshift the band centers of the Q and B (or Soret) bands. The most-widely applicable approach is the fusion of aromatic rings onto the β -pyrrole carbon atoms. Although there have been a large number of reports on the effect of peripheral-fused-ring expansion on conventional tetrapyrrole porphyrins,^[14] the fused-ring expansion of core-modified porphyrins has only been studied to a limited extent.^[15] Herein, we report an in-depth analysis of the optical properties of porphyrinoids with Group 16 heteroatoms, by replacing the two protonated pyrrole nitrogen atoms, and we explore the effect of fused-ring-expansion, the incorporation of addition-

[a] Dr. H.-J. Xu,⁺ Dr. D. Wu,⁺ Dr. Z.-L. Xue,⁺ Prof. Z. Shen
State Key Laboratory of Coordination Chemistry
Nanjing National Laboratory of Microstructures
School of Chemistry and Chemical Engineering
Nanjing University, Nanjing 210093 (P.R. China)
Fax: (+86) 25–8331–4502
E-mail: zshen@nju.edu.cn


[b] Dr. J. Mack, Prof. N. Kobayashi
Department of Chemistry, Graduate School of Science
Tohoku University, Sendai 980–8578 (Japan)
Fax: (+81) 22–795–7719
E-mail: nagaok@m.tohoku.ac.jp

[c] Dr. A. B. Descalzo, Dr. K. Rurack
Division 1.9 Sensor Materials
BAM Federal Institute for Materials Research and Testing
Richard-Willstätter-Strasse 11, 12489 Berlin (Germany)
Fax: (+49) 30–8104–1157
E-mail: knut.rurack@bam.de

[d] Dr. J. Mack
Current address: Department of Chemistry
Rhodes University, Grahamstown (South Africa)

[e] Dr. A. B. Descalzo
Current address: Department of Organic Chemistry
Faculty of Chemical Sciences
Complutense University of Madrid
Avda. Complutense s/n, 28040 Madrid (Spain)

[⁺] These authors contributed equally to this work.

 Supporting information for this article is available on the WWW under <http://dx.doi.org/10.1002/chem.201200956>.

al pyrrole moieties, ligand nonplanarity, and the electron-donating properties of *meso*-aryl substituents on their electronic structures.

We have recently demonstrated that *meso*-tetraphenyltetraphenanthroporphyrins (TPTPhenPs) have remarkably redshifted B bands, due to the introduction of peripheral-fused phenanthrene rings.^[16] Similar results had previously been reported by Lash and co-workers for compounds with peripheral-fused acenaphthalene rings.^[10a,b] This work prompted us to explore the effect of introducing fused-phenanthrene rings at the β -pyrrole carbon positions of core-modified porphyrins to synthesize new porphyrinoids with optical properties in the NIR region that would be suitable for use in various applications. For example, water-soluble core-modified porphyrins have recently emerged as potentially useful agents for photodynamic therapy (PDT).^[17] Herein, we report the synthesis of N_2O_2 , N_2S_2 , N_2Se_2 , and N_2Te_2 tetraphenyldiphenanthroporphyrins (this terminology, used throughout, refers to the four core atoms on the inner perimeter of the π -system that can coordinate a central metal atom; Figure 1 and the Supporting Information, Figure S1), in which Group 16 heteroatoms replace the protonated pyrrole nitrogen atoms along the y axis and peripheral-fused-phenanthrene rings are substituted onto the pyrrole moieties on the x axis. These macrocycles can potentially stabilize metals in unusual oxidation states. For example,

5,10,15,20-tetraphenyl-21-oxaporphyrin can stabilize nickel(I),^[18] which is not possible with 5,10,15,20-tetraphenylporphyrin (TPP), due to the presence of an N_3O (rather than an N_4) core. The use of thia- and oxaporphyrin as terminology to describe core-modified porphyrinoids was originally introduced by Johnson and co-workers^[19] and is now well-established in the literature^[20] despite the fact that it would normally only be applied to the replacement of a carbon atom rather than a nitrogen atom. Most of the recent research on core-modified porphyrins has focused on N_3S and N_2S_2 compounds;^[20] there have been relatively few reports of compounds that contain O, Se, and Te atoms.

The influence of the heteroatoms on the electronic structure and optical properties of the porphyrinoids is examined in-depth based on TD-DFT calculations and magnetic circular dichroism (MCD) and fluorescence measurements (Figure 1). MCD measurements were carried out on a series of compounds with *n*-hexadecyloxy groups incorporated at the para positions of the phenyl substituents (N2Y2-OC16H33), since this enhances the solubility in optically transparent solvents. Electron-donating OMe and $N(CH_3)_2$ groups (N_2Se_2 -OMe and N_2Se_2 -NMe₂) and electron-withdrawing F atoms (N_2O_2 -F and N_2S_2 -F) have been used to examine the extent to which the aryl substituents can be used to fine-tune the optical properties, whilst Cl, Br, and I atoms (N_2O_2 -Cl, N_2O_2 -Br, and N_2O_2 -I) were introduced so that the

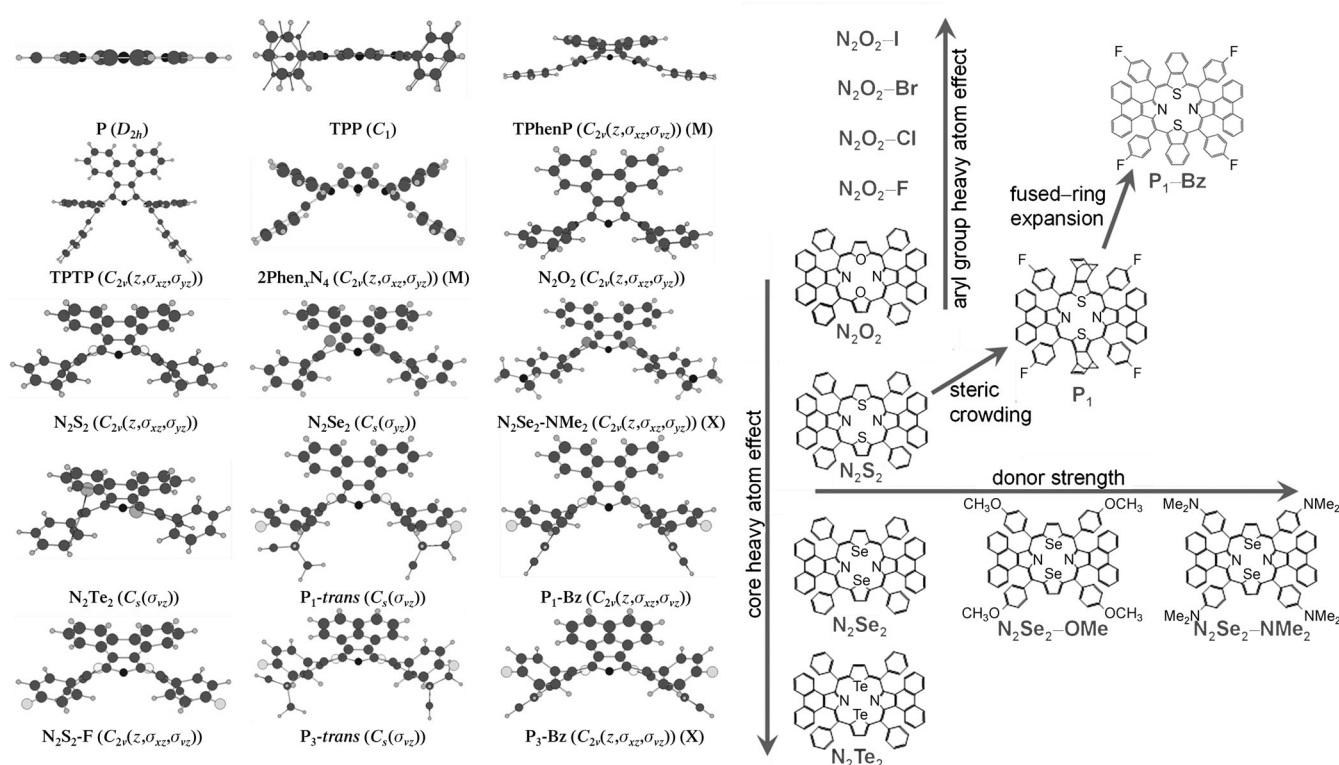


Figure 1. Left: Cross-section views in the yz plane of the B3LYP-optimized geometries of **P**, **TPP**, **TPTPhenP** (**TPTTP**), **N₂O₂**, **N₂S₂**, **N₂Se₂**, **N₂Te₂**, **N₂S₂-F**, **P₁**, **P₁-Bz**, and **P₃**, model compound structures (M) of **TPhenP** and **2Phen₂N₄**, and the X-ray structures (X) of **N₂Se₂-NMe₂** and **P₃-Bz**, based on the use of 6-31G(d) basis sets (3-21G** basis sets for **N₂Te₂**). Only the *trans* isomers are shown with respect to the BCOD groups in structures **P₁** and **P₃**. The axes are orientated such that the y and z axes lie horizontally and vertically in the plane of the page, respectively. For cross-section views in the xy and xz planes, see the Supporting Information. Right: Key trends to be analyzed by MCD and/or fluorescence spectroscopy.

relative influence of the heavy-atom effect and core modification on the emission properties could be compared. The effect of forming ABAB structures with differing types of peripheral-fused-ring expansion has been explored by synthesizing core-modified diphenanthro- (**P**₁ and **P**₁-**Bz**_y) and diacenaphthoporphyrins (**P**₃ and **P**₃-**Bz**_y; Figure 1 and the Supporting Information, Figure S1), which have fused bicyclo[2.2.2]octadiene (BCOD) and benzene rings along the y axis.

Synthesis of core-modified porphyrins: The synthesis of monohetero- and diheteroporphyrins was pioneered by Ulman and Manassen in the mid-1970s, based on a reaction between a diarylfuran/diarylthiophene diol and a pyrrole to form a porphyrinoid compound.^[21] In recent years, Ono and co-workers developed a breakthrough synthesis of pure π -expanded porphyrinoids^[22] and benzo[*c*]heterocyclic oligomers^[23,24] that was based on the tetramerization of BCOD-fused pyrroles to afford peripherally substituted porphyrins, which can subsequently be converted into tetrabenzoporphyrins in quantitative yield by heating at 200 °C.^[25] A series of core-modified tetrabenzoporphyrins, in which one or both of the protonated pyrrole nitrogen atoms were replaced with oxygen/sulfur atoms by using BCOD-fused furan and thiophene, respectively, were successfully synthesized.^[23,26] The same synthetic approach is adopted herein to synthesize **P**₁-**Bz**_y and **P**₃-**Bz**_y based on the retro-Diels–Alder reaction of **P**₁ and **P**₃, respectively, which are formed from a BCOD-fused diarylthiophene diol with either a phenanthro- or acenaphtho-fused pyrrole. The replacement of pyrrole moieties by other heterocycles, such as furans, thiophenes, selenophenes, or tellurophenes, leads to the formation of new classes of core-modified porphyrinoids. Ulman and Manassen's methodology^[21] is used to form **N**₂**O**₂, **N**₂**S**₂, **N**₂**Se**₂,

and **N**₂**Te**₂ compounds by using the corresponding non-BCOD fused furan, thiophene, selenophene, tellurophene, dithiophene, and diselenophene diols with a phenanthro-fused pyrrole precursor. Aryl groups with different *para*-substituents can be readily introduced during the preparation of the diols. For full details, see the Experimental Section.

X-ray structures are reported for **N**₂**Se**₂-**NMe**₂ and **P**₃-**Bz**_y, which fit the tetragonal *P*4(2)/*nmc* and monoclinic *P*21/*n* space groups, respectively (Figure 2 and the Supporting Information, Figure S2 and Table S1). Steric hindrance between the *meso*-phenyl substituents and the peripheral-fused-ring moieties resulted in a significant saddling distortion of the π -system (see the Supporting Information, Tables S2 and S3), which rotated the *meso*-phenyl groups into the plane that was formed by the four *meso*-carbon atoms on the inner ligand perimeter. Recent studies on core-modified tetrabenzoporphyrins^[15] and **TPTPhenPs**^[16] have demonstrated that the results of DFT geometry optimizations are very similar to those obtained by X-ray crystallography when steric hindrance between peripheral-fused rings results in severe ligand folding, due to the lack of conformational flexibility. Therefore, the observed trends in the experimental data of the core-modified structures synthesized herein can be readily compared to those predicted by theoretical calculations for the B3LYP-optimized geometries, even in the absence of X-ray structures.

Electronic structure of porphyrinoids: Many key breakthroughs in understanding the electronic structure of porphyrinoids have been derived from MCD spectroscopy.^[27] Analysis of the MCD spectra is based on the three Faraday terms: \mathcal{A}_1 , \mathcal{B}_0 , and \mathcal{C}_0 . Because there are no three-fold or higher axes of symmetry, the spectra of the core-modified

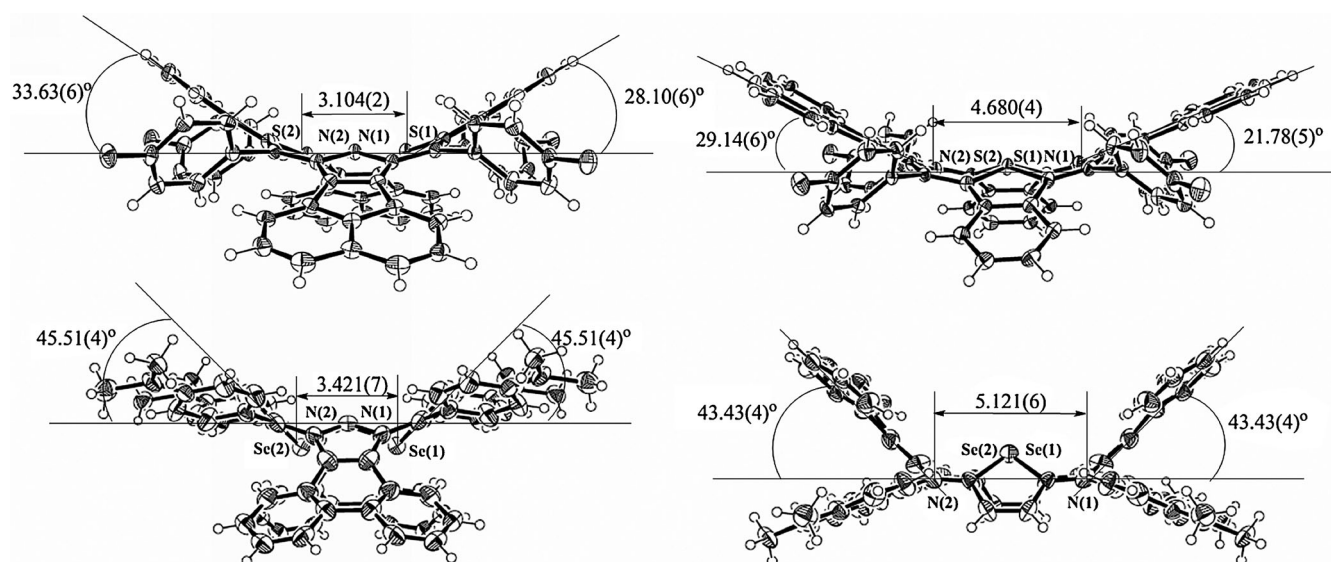


Figure 2. Crystal structures of a) **P**₃-**Bz**_y (top) and b) **N**₂**Se**₂-**NMe**₂ (bottom); thermal ellipsoids are set at 50% probability. Phenyl groups and solvent molecules are omitted for clarity.

porphyrinoids reported herein are completely dominated by positively and negatively signed and Gaussian-shaped Faraday \mathcal{B}_0 terms. The application of TD-DFT techniques to MCD spectroscopy is still being developed.^[28,29] Theoretical approaches based on semi-empirical theoretical techniques, such as Michl's perimeter model^[30] and Gouterman's 4-orbital model,^[31] continue to play an important role in the interpretation of the optical spectra of porphyrinoids. These approaches provide readily accessible conceptual frameworks for rationalizing and predicting key trends in the spectroscopic data. The orbital angular momentum (OAM) properties of the π -MOs of porphyrinoids can typically be described in terms of an $M_L = 0, \pm 1, \pm 2, \pm 3, \pm 4, \pm 5, \pm 6, \pm 7, 8$ sequence in the magnetic quantum number, in ascending energy, for those π -MOs which are associated with a D_{16h} symmetry of the $C_{16}H_{16}^{2-}$ parent perimeter for the 18 π electrons on the 16-atom inner ligand perimeters of conventional tetrapyrrole porphyrinoids. This perimeter-model approach is based on the fact that heteroaromatic π -systems maintain their OAM properties upon symmetry-lowering structural perturbations. The nodal patterns of the four frontier π -MOs of the free-base porphyrin (**P**), **TPP**, **TPTPhenP**, **N₂O₂**, **N₂S₂**, **N₂Se₂**, **N₂Te₂**, **P₁**, **P₁-Bz_y**, **P₃**, and **P₃-Bz_y** are consistent with a $C_{16}H_{16}^{2-}$ parent perimeter (see the Supporting Information, Figure S3). Because an incident photon can only provide one quantum of orbital angular momentum, optical spectroscopic data of the porphyrinoids can be assigned in the context of Gouterman's 4-orbital model^[31] to an allowed B band (" $\Delta M_L = \pm 1$ ") and a forbidden Q band (" $\Delta M_L = \pm 9$ "), which arise from the four spin-allowed transitions that link the HOMOs ($M_L = \pm 4$) and the LUMOs ($M_L = \pm 5$; Figure 3). When the symmetry is lowered to form a porphyrinoid, there is a mixing of the allowed and forbidden properties of the Q and B excited states, but the OAM properties of the frontier π -MOs of the parent perimeter are largely retained.^[30] In Michl's perimeter model (Figure 4), the excited-state magnetic moments of the states that arise from the Q and B transitions of the parent perimeter are referred to as μ^- and μ^+ , respectively. The μ^- moment is relatively small and is associated with the net charge circulation on the perimeter upon electronic excitation when the circulation of the excited electron in the LUMO level and the hole that is left in the HOMO level are both taken into consideration. The μ^+ moment is much larger due to a reversal of the handedness properties of the circulation of the excited electron. In the case of the parent D_{16h} or D_{22h} symmetry of the hydrocarbon perimeters discussed herein, the Q_{00} bands would be fully electric-dipole forbidden and the sign and intensity of the \mathcal{A}_1 term that arises from the B transition would be exclusively determined by the far-weaker μ^- moment. When the symmetry is lowered to form a porphyrin with D_{4h} symmetry, there is an increase in the degeneracy of the MOs that are derived from the HOMO level of the parent perimeter but not of those from the LUMO level (the magnitudes of these splittings are referred to as the Δ HOMO and Δ LUMO values in the context of Michl's model). Michl^[30] demonstrated that the

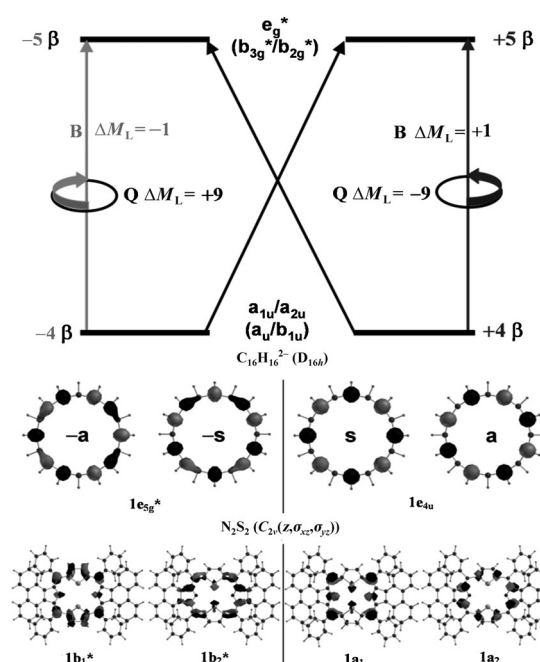


Figure 3. Top: Origin of the Q and B bands in Gouterman's 4-orbital model.^[31] In the context of a free-electron model, the doubly degenerate HOMO and LUMO of the inner cyclic polyene perimeter of $C_{16}H_{16}^{2-}$ exhibit angular momenta of ± 4 and ± 5 , respectively. Configurational interaction between the four possible spin-allowed one-electron transitions results in forbidden Q bands and allowed B bands. When the symmetry is lowered to D_{2h} , the zero-field splitting of the excited states split the Q and B bands into their x- and y-polarized components. Bottom: The four frontier π -MOs of the $C_{16}H_{16}^{2-}$ parent perimeter and **N₂S₂** were found to exhibit $M_L = \pm 4, \pm 5$ nodal patterns in the differences in phase on the inner cyclic perimeter of the π -system as would be anticipated on the basis of Gouterman's 4-orbital^[31] and Michl's perimeter^[30] model (Figure 4). The nodal patterns were generated from the Gaussian checkpoint files using the CS Chem3D program at the 0.04 a.u. energy level of the isosurface value for electrostatic potential. In the context of Michl's perimeter model, the MOs with nodal planes along the y axis are referred to as "a" and "–a" MOs, whereas those with large MO coefficients are referred to as "s" and "–s" MOs. The nodal patterns for all of the compounds in Figure 1 are provided in the Supporting Information, Figure S3.

degree of mixing (α) and the magnitude of the induced magnetic dipole moments, which are associated with the first-derivative-shaped Faraday \mathcal{A}_1 terms (the intensity of the \mathcal{A}_1 term is associated with the differential absorbance of left- and right-polarized light, due to the Zeeman splitting of orbitally degenerate excited states) of the Q and B bands (μ_Q, μ_B), based on the observed dipole strengths (D_0), can be predicted by Equations (1)–(3).

$$D_{0(Q)}/D_{0(B)} = \tan^2 \alpha \quad (1)$$

$$\mu_B = \pm(\cos^2 \alpha)\mu^- \pm (\sin^2 \alpha)\mu^+ \quad (2)$$

$$\mu_Q = \pm(\sin^2 \alpha)\mu^- \pm (\cos^2 \alpha)\mu^+ \quad (3)$$

In the case of low-symmetry chromophores, in which Δ HOMO and Δ LUMO $\neq 0$, the MCD spectra are dominat-

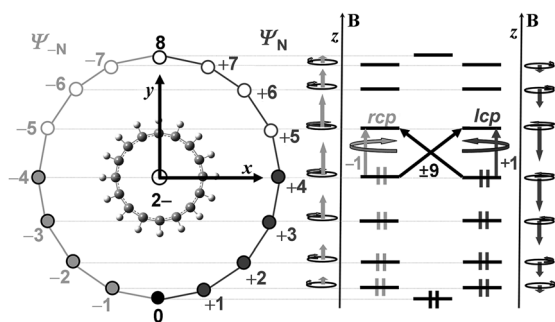


Figure 4. Left: Michl's perimeter model^[30] for $C_{16}H_{16}^{2+}$. The circle represents the clockwise and counterclockwise motions of the π -system electrons on the inner ligand perimeter, thereby generating the M_L value for each complex π -MO. Right: The alignment and magnitude of the magnetic moments that are induced by the electron motion within each π -MO can be predicted based on the right-hand rule and linear combination of atomic orbital (LCAO) calculations. The moments aligned along the z axis with/against the applied field are shown schematically.^[31] Right- and left-handedness are defined within classical optics by looking towards the light source of the CD spectrometer (lcp and rcp = left and right circularly polarized light, respectively).

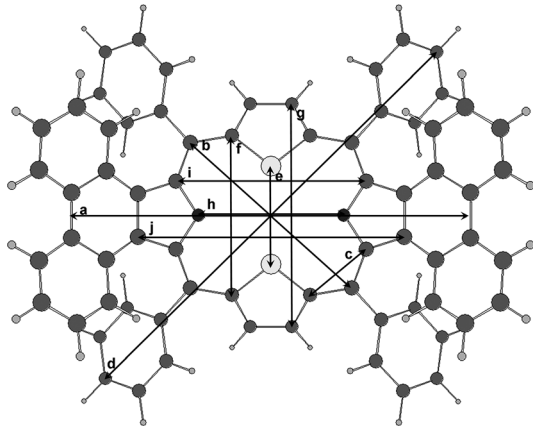
ed by Gaussian-shaped Faraday \mathcal{B}_0 terms. The intensity of the \mathcal{B}_0 term arises from the field-induced mixing of states that are linked by a magnetic dipole transition moment; thus, a coupled pair of oppositely signed bands replaces the derivative-shaped \mathcal{A}_1 term, due to the zero-field splitting of the Q and B excited states. Michl^[30] has demonstrated that, in the context of aromatic π -systems, such as porphyrinoids, the differential absorbance of left- and right-polarized light (and, hence, the ordering of the MCD signs for the Qx, Qy, Bx, and By bands) by the excited states of aromatic π -systems, such as porphyrinoids, is related to the alignment of the induced magnetic moments with or against the axis of light propagation and the applied field, and is primarily determined by the relative magnitudes of the $\Delta HOMO$ and $\Delta LUMO$ values. When a structural perturbation introduces a large $\Delta HOMO$ or $\Delta LUMO$ value, the circulation of the charge on the perimeter is hindered. Therefore, the relative magnitudes of the $\Delta HOMO$ and $\Delta LUMO$ values determine whether the circulation of the excited electron in the LUMO level or that of the hole that is left in the HOMO level is the dominant factor in conserving the quantum of orbital angular momentum that is provided by the incident photon of left- or right-circularly polarized light. Ampere's rule (right-hand rule) for conventional current flow in a solenoid^[27] can be used to demonstrate that, when $\Delta HOMO > \Delta LUMO$ and electronic-charge circulation in the LUMO predominates, the ordering of the signs of MCD intensity for the \mathcal{B}_0 terms that are associated with the Q and B bands is $-, +, -, +$, in ascending energy terms. In contrast, when $\Delta LUMO > \Delta HOMO$ and the circulation of the positive charge that is associated with the hole that is left in the HOMO is the dominant factor, the sequence reverses to $+, -, +, -$.

Results and Discussion

Recently, we showed that **TPTPhenP** has the most redshifted B band of any radially symmetric fused-ring-expanded porphyrinoid.^[16] Although **TPTPhenPs** are of considerable academic interest, their severely saddled structure hinders the coordination of a central metal and lowers the stability of these compounds relative to almost-planar porphyrinoids. Therefore, further structural modification is required to form porphyrinoids that are suitable for practical applications. The goal of our research is the synthesis of low-symmetry phenanthroporphyrins that retain the markedly redshifted Q and B bands of **TPTPhenP**, but with π -systems that are not as severely folded. Herein, our main strategy to try to meet these goals was to synthesize a series of core-modified porphyrins in which the protonated pyrrole rings on the y axis were replaced by furan, thiophene, selenophene, and tellurophene moieties to form N_2O_2 , N_2S_2 , N_2Se_2 , and N_2Te_2 , respectively. Significant redshifting of the Q and B bands has been reported previously for core-modified porphyrins.^[15] Because there are no fused phenanthrenes attached to the furan, thiophene, selenophene, and tellurophene moieties, there is a markedly lower degree of folding of the π -system (Table 1). The electronic structures of these core-modified tetraphenyldiphenanthroporphyrins are expected to exhibit properties that are similar to those of **TPTPhenPs**, due to the nature of the structural perturbations. We recently reported an in-depth analysis of the optical properties of core-modified tetrabenzoporphyrins,^[15] in which we demonstrated that a core-modified tetraphenyltetrabenzodithiaporphyrin that contained two thiophene moieties, which lay on the y axis, and two benzo groups, which were fused to the pyrrole moieties along the x axis (**2Bz_x**; Figure 5), retained many of the optical properties of the parent hydrocarbon perimeter, because $\Delta HOMO \approx \Delta LUMO$. Therefore, their OAM properties were similar to those of—what Michl referred to as—double soft MCD chromophores,^[30] such as tetraphenyltetraacenanthroporphyrin (**TPTANP**), for which $\Delta HOMO \approx \Delta LUMO \approx 0$. Markedly redshifted B bands tend to be observed for porphyrinoid chromophores of this type, because the Q and B bands retain their ideal forbidden and allowed properties and there is very limited configurational interaction between the B and higher-energy $\pi\pi^*$ states.^[14]

Michl's perimeter model: To perform the rational design of new porphyrinoids, the effect of different structural perturbations, such as fused-ring-expansion, must be fully understood. Michl's perimeter model^[30] can be used to rationalize how different peripheral-fused rings affect the HOMO–LUMO band gap and the $\Delta HOMO$ and $\Delta LUMO$ values and, hence, the spectroscopic properties (Figure 6). Although theoretical calculations can be used to derive quantitative values for the energies of the four frontier π -MOs, predictions of the magnitudes of the $\Delta HOMO$ and $\Delta LUMO$ values can also be made based on a qualitative consideration of the nodal patterns of the four frontier π -MOs, due to

Table 1. Trends in the key distances [Å] in the molecular structures of **P**, **TPP**, **TPhenP**, **TPTPhenP**, **N₂O₂**, **N₂O₂-OMe**, **N₂S₂**, **N₂S₂-OMe**, **N₂S₂-F**, **N₂Se₂**, **N₂Se₂-OMe**, **N₂Te₂**, **P₁-Bz_y**, and **P₃-Bz_y**, the *trans* and *cis* isomers of **P₁** and **P₃**, and the X-ray structures (X) of **P₃-Bz_y** and **N₂Se₂-NMe₂**.



	<i>a</i>	<i>b</i>	<i>c</i>	<i>d</i>	<i>e</i>	<i>f</i>	<i>g</i>	<i>h</i>	<i>i</i>	<i>j</i>
P	—	6.88	2.50	—	4.24	5.79	8.52	4.06	5.79	8.52
TPP	—	6.93	2.50	15.56	4.22	5.78	8.50	4.08	5.73	8.53
TPhenP	13.14	6.80	2.52	—	4.19	5.70	8.36	4.03	5.61	8.32
TPTPhenP	9.67	6.75	2.46	15.36	4.16	5.20	6.90	4.09	5.22	6.87
N₂O₂	10.88	6.72	2.47	15.07	4.22	5.39	7.33	4.01	5.31	7.38
N₂O₂-OMe	10.89	6.73	2.47	15.06	4.23	5.40	7.32	4.02	5.31	7.38
N₂S₂	13.10	7.10	2.48	15.21	3.20	5.20	7.27	4.78	6.24	8.75
N₂S₂-OMe	12.97	7.10	2.48	15.27	3.23	5.20	7.23	4.79	6.23	8.70
N₂S₂-F	13.09	7.10	2.48	15.18	3.21	5.20	7.26	4.78	6.24	8.74
N₂Se₂	13.(33/6)	7.18	2.(47/8)	15.17	3.16	5.18	7.14	4.89	6.(35/9)	8.(90/3)
N₂Se₂-OMe	13.14	7.18	2.47	15.22	3.18	5.20	7.10	4.91	6.35	8.83
N₂Se₂-NMe₂	12.99	7.19	2.47	15.34	3.20	5.21	7.09	4.93	6.34	8.77
N₂Se₂-NMe₂ (X)	12.30	7.26	2.47	15.55	3.42	5.22	7.20	5.12	6.42	8.41
N₂Te₂	13.(76/90)	7.31	2.(45/7)	15.17	3.45	5.15	6.83	5.00	6.(52/60)	9.(21/9)
P₁-trans	12.25/6	7.09	2.47	15.40	3.53	5.16	6.82	4.79	6.11	8.37
P₁-cis-sp²	12.32	7.09	2.47	15.40	3.54	5.17	6.81	4.78	6.11	8.39
P₁-cis-sp³	12.19	7.09	2.47	15.41	3.51	5.15	6.84	4.80	6.11	8.35
P₁-Bz_y	12.02	7.06	2.47	15.45	3.37	5.13	6.88	4.77	6.05	8.23
P₃-trans	—	7.15	2.50	15.67	3.15	5.39	7.68	4.77	6.25	8.82
P₃-cis-sp²	—	7.15	2.50	15.67	3.15	5.39	7.69	4.76	6.25	8.84
P₃-cis-sp³	—	7.15	2.50	15.66	3.15	5.38	7.67	4.77	6.24	8.80
P₃-Bz_y	—	7.12	2.49	15.65	3.13	5.37	7.70	4.73	6.17	8.67
P₃-Bz_y (X)	—	7.(07/10)	2.49	15.(52/5)	3.13	5.(37/8)	7.(75/7)	4.64	6.(15/7)	8.(75/6)

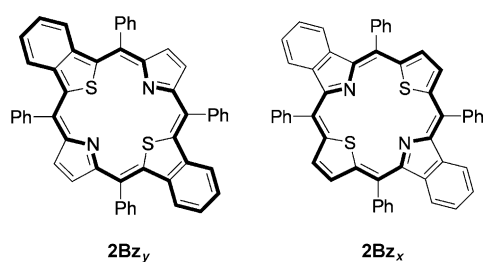


Figure 5. Structures of 5,10,15,20-tetraphenyldibenzo[*b,l*]-21,23-dithiaporphyrin (**2Bz_y**) and 5,10,15,20-tetraphenyldibenzo[*g,q*]-21,23-dithiaporphyrin (**2Bz_x**), which are core-modified tetrabenzoporphyrins with **N₂S₂** structures. The pathway of the dominant ring current, which was observed by NMR spectroscopic analysis, is shown in bold.^[15] The core-modified tetraphenyldiphenanthroporphyrins reported herein have structures that are similar to that of **2Bz_x** (with the exception of **P₁-Bz** and **P₃-Bz**).

the differing effects of fused-ring expansion with acenaphthalene, phenanthrene, and benzene rings on the four fron-

tier π -MOs of **P**. The effect of adding fused rings onto the periphery of the porphyrin ligand can be readily understood with reference to the effect of symmetry-lowering structural perturbations on the relative energies of four key frontier π -MOs that are primarily associated with the 16-atom 18π -electron cyclic polyene on the inner ligand perimeter. The perimeter-model approach often enables accurate predictions to be made about key aspects of the electronic structure and optical spectroscopic properties, based on a qualitative consideration of the alignment of the nodal planes of the four frontier π -MOs. In the context of $4N+2$ π -electron systems, the HOMO level has $2N$ nodal planes, whilst the LUMO level has $2(N+1)$, thereby effectively forming either an octagon or a decagon on the 16-atom inner perimeter (Figure 7). Under the D_{2h} symmetry of porphyrin compounds, the alignment of the $2N$ nodal planes of the HOMO level is defined (for symmetry reasons) by the mirror planes that run through the pyrrole nitrogen atoms. The alignment of the y axis through the protonated set of

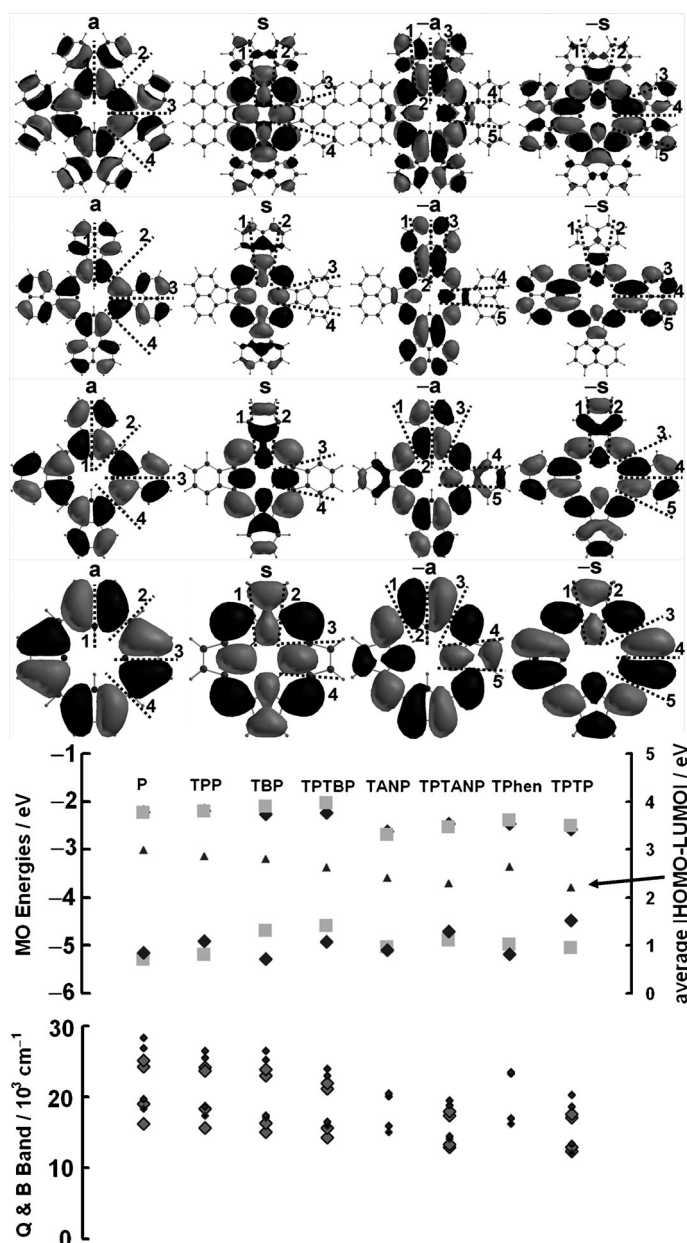


Figure 6. Center: MO energies of the frontier π -MOs of **P**, **TPP**, **TBP**, **TPTBP**, **TANP**, **TPTANP**, **TPhenP** (**TPhen**), and **TPTPhenP** (**TPTP**) that were obtained from TD-DFT calculations with the B3LYP functional by using 6-31G(d) basis sets. The “a” and “-a” MOs with nodal planes on the protonated pyrrole nitrogen atoms ($1a_u$ and $1b_{2g}^*$) are denoted by gray squares, whilst the “s” and “-s” MOs ($1b_{1u}$ and $1b_{3g}^*$), with significant MO coefficients on these atoms, are denoted by black diamonds. The nodal patterns (top), arranged in an ascending order, of the “a”, “s”, “-a”, and “-s” MOs of **P**, **TBP**, **TANP**, and **TPhenP** are at an isosurface of 0.01. The average HOMO–LUMO band gap values, which take into account all four MOs that are derived from the HOMO and LUMO of the parent perimeter, are denoted by small dark-gray triangles plotted against a secondary axis (center). The observed trends closely mirror those in the observed (large light-gray diamonds) and calculated energies (small black diamonds) of the Q and B bands (bottom).

pyrrole nitrogen atoms is used to define the identity of the MO with $M_L=0$ (Figure 7). The $1a_{1u}$ and $1a_{2u}$ MOs have nodes and antinodes at these positions on the inner ligand

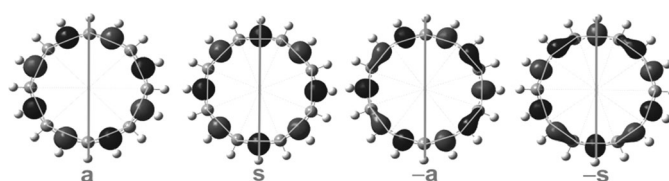


Figure 7. In the context of Michl’s perimeter model,^[30] the nodal properties of the frontier π -MOs on the inner perimeter of the porphyrinoid ligands can be understood based on a parent $C_{16}H_{16}^{2-}$ hydrocarbon. The $2N$ nodal planes of the MOs which are associated with the HOMO of the $4N+2$ ($N=4$) parent perimeter form octagonal patterns on the perimeter because there are planes running through alternating sets of atoms. In contrast, the $2(N+1)$ nodal planes of the LUMO-level MOs form a decagon in which the planes (with the exception of those lying on either the x or y axis) do not coincide with the atomic positions. When there is a symmetry-lowering structural perturbation, such as fused-ring expansion or core modification, the nodal patterns are determined by the alignment of the yz plane of symmetry. In this context, Michl introduced “a”, “s”, “-a”, and “-s” nomenclature to describe the four frontier π -MOs, based on whether there is a nodal plane (a and -a) or an antinode (s and -s), corresponding to the $M_L=0$ in Figure 4. Once the alignment of the nodal planes has been clearly defined, the effect of different structural perturbations can be readily conceptualized on a qualitative basis through a consideration of the relative size of the MO coefficients on each atom on the perimeter.

perimeter and are referred to as the “a” and “s” MOs, respectively, on this basis, in the context of Michl’s perimeter model (Figure 7). In both of these MOs, eight atoms of the inner perimeter either lie on or very close to nodal planes, whilst the other eight lie on or very close to antinodes, with the phase sign changing as each nodal plane is crossed; thus the nodal patterns of the “a” and “s” MOs are radially symmetric. The $1b_{2g}^*$ and $1b_{3g}^*$ MOs are referred to as the “-a” and “-s” MOs, because there is, respectively, a nodal plane and an antinode on the pyrrole nitrogen atom on the y axis, which is regarded as the $M_L=0$ MO. The “a” and “s” MOs do not have radial symmetry because a decagon (rather than an octagon) is formed by the nodal planes on the 16-atom perimeter. Thus the twelve atoms that do not lie on the x and y axes no longer lie on a nodal plane or an antinode.

Once the alignment of the nodal planes on the inner ligand perimeter in each of the four frontier π -MOs has been defined, it becomes easy to determine the effect of various structural perturbations on the energy of the MOs. In the context of porphyrin compounds, the “a” and “s” MOs remain (accidentally) almost degenerate. The net stabilizing effect on the “s” MO, due to the increased electronegativity of the four pyrrole nitrogen atoms at the nodes of the “a” MO is matched by the stabilizing effect on the “a” MO of adding the four peripheral C_2H_2 bridges at nodes of the “s” MO (Figure 6), based on a strong bonding interaction between the “a” MO of the inner ligand perimeter and what can be viewed as four antibonding ethylene MOs. Michl^[30] has demonstrated that the effect on the MO energies of introducing bridging atoms is primarily determined by the size and sign of the relative phase of the MO coefficients on the perimeter atom on which the bridge is attached and on the

first atom of the bridge, because this result determines whether there is a stabilizing bonding interaction or a destabilizing antibonding interaction. When the bridges consist of an even number of atoms, the four frontier π -MOs of the parent perimeter will usually still be the HOMO–1, HOMO, LUMO, and LUMO+1 of the expanded π -system.^[30c] In the case of metal complexes, symmetry considerations dictate that the “–a” and “–s” MOs remain degenerate, because only the degeneracy of the $M_L = \pm 2, \pm 4$, and ± 6 MOs is lifted on moving from D_{16h} to D_{4h} symmetry (Figure 6). However, in the context of free-base compounds, the introduction of protonated pyrrole nitrogen atoms along the y axis results in a slight increase in the degeneracy of the LUMO level. In the “–a” and “–s” MOs, the differing interactions with the peripheral ethylene bridges along the x and y axes are broadly similar and only differ in their relative orientation; thus, a minor lifting of the degeneracy of the LUMO is anticipated based on the relative size of the MO coefficients on the protonated and nonprotonated pyrrole nitrogen atoms.

Fused-ring expansion with benzene rings: When fused benzene rings are added onto the porphyrin ligand in a radially symmetric manner to form tetrabenzoporphyrin (**TBP**), there is an antibonding interaction between the “a” MO and the C_4H_4 bridge at all eight positions of attachment, thereby resulting in a marked destabilization of the MO energy (Figure 6). In contrast, there is a slight stabilization of the “s” MO, due to a weak bonding interaction. The energies of the “–a” and “–s” MOs of the free-base **TBP** remain largely unchanged, because the stabilizing interaction that is introduced along one axis is balanced by the destabilizing interaction along the other, so that the low Δ LUMO value of **P** is retained. The marked destabilization of the “a” MO leads to a narrowing of the HOMO–LUMO band gap and the introduction of a significant Δ HOMO value, so there is a redshift and intensification of the Q band. Only a relatively minor redshift of the B band is observed, due to an increased interaction between the B and higher-energy $\pi\pi^*$ states.^[14] Marked differences are observed in the optical spectroscopic properties of **2Bz_x** and **2Bz_y**,^[15] because there is no longer a balancing of the stabilizing and destabilizing effects when peripheral-fused rings are only added along one axis. In the context of **2Bz_x**, the stabilizing effect of benzo substitution along the x axis on the “–a” MO is similar to that of a stabilizing effect on the “–s” MO, due to core modification, so there is a relatively low Δ LUMO value. In contrast, the Δ LUMO value increases markedly in the context of **2Bz_y**, in which benzo substitution results in a stabilization of the “–s” MO.

Fused-ring expansion with acenaphthalene and phenanthrene rings: The radially symmetric fused-ring expansion of **P** with acenaphthalene moieties to form tetraacenaphthoporphyrin (**TANP**) has a markedly different effect on the relative energies of the four frontier π -MOs. A destabilization of both the “a” and “s” MOs is anticipated, because there are anti-

bonding interactions between the β -carbon atoms of the pyrrole moieties of **P** and the two carbon atoms of the peripheral $C_{10}H_6$ bridging units to which they are attached; however, this destabilization is relatively minor in magnitude, because the MO coefficients on the fused acenaphthalene rings are relatively low. In contrast, there is a marked stabilization of the “–a” and “–s” MOs because there are strong bonding interactions along the y and x axes, respectively, which involve relatively large MO coefficients. Therefore, the Δ HOMO value of **TANP** is significantly lower than that predicted for **TBP** and there is a markedly narrower HOMO–LUMO band gap. This result accounts for the unusually large shift of the Q and B bands reported by Lash and others,^[10a,b] which results in an unusually large redshift of the B band and spectroscopic properties, which, in other regards, are broadly similar to those of the parent porphyrin compound, because Δ HOMO \approx Δ LUMO \approx 0. A similar pattern is observed when fused phenanthrenes are added to form tetraphenanthroporphyrin (**TPhenP**), but the stabilization of the “–a” and “–s” MOs is not as large as that observed for **TANP** and, therefore, a larger HOMO–LUMO band gap is predicted. When phenyl substituents are added at the *meso*-carbon atoms to form tetraphenyltetrabenzoporphyrin (**TPTBP**), **TPTANP**, and **TPTPhenP**, there is a destabilization of the “s” MO, due to the large coefficients on these atoms. This typically results in a decrease in both the Δ HOMO value and in the intensity of the Q band, as well as a redshift of both the Q and B bands. No significant destabilization of the “a” MO is anticipated, because the *meso*-carbon atoms lie on nodal planes. In the context of **TPTANP**, the destabilization of the “s” MO results in a soft MCD chromophore with Δ HOMO \approx Δ LUMO \approx 0. However, a larger Δ HOMO value is predicted in the context of **TPTPhenPs**, because increased steric hindrance rotates the phenyl groups almost into the plane of the inner perimeter of the π system. This results in a more-pronounced redshift and a higher intensity of the Q band than is observed with **TPTANPs**.^[14]

B3LYP geometry optimizations and MO energies: The predicted B3LYP-optimized geometries for **P**, **TBP**, **TPhenP**, **TPTPhenP**, **N₂O₂**, **N₂S₂**, **N₂Se₂**, **N₂Te₂**, **P₁**, **P₁-Bz_y**, **P₃**, and **P₃-Bz_y** are shown in Figure 1, along with the non-core-modified tetraphenyldiphenanthroporphyrin (**2Phen_xN₄**) parent compound for the **N₂O₂**, **N₂S₂**, **N₂Se₂**, and **N₂Te₂** series. Peripheral substitution with fused phenanthrene and acenaphthalene ring systems results in severe saddling of the tetraphenylporphyrins due to steric hindrance with the *meso*-aryl substituents.^[10,14–16] In the case of **TPTPhenP**, this results in a fixed $C_{2v}(z, \sigma_{xz}, \sigma_{yz})$ geometry because the phenyl groups can no longer freely rotate. When the protonated pyrroles are replaced by Group 16 atoms, by introducing furan, thiophene, selenophene, or tellurophene moieties along the y axis, the structures remain highly nonplanar but the saddling distortion of the π system steadily diminishes as the heteroatoms become progressively larger on going from O to S and then to Se and Te to form **N₂O₂**, **N₂S₂**, **N₂Se₂** and **N₂Te₂** (Table 1).

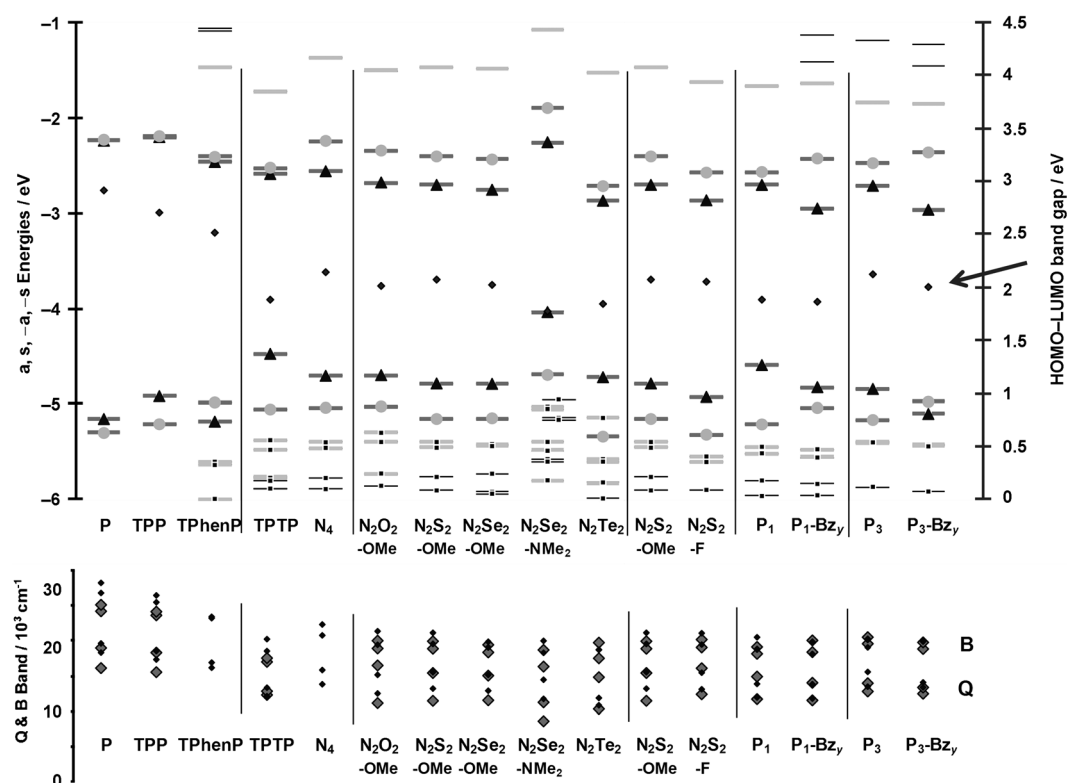


Figure 8. Top: MO energies of free-base **P**, **TPP**, **TPhenP**, **TPTPhenP** (**TPTP**), **2Phen_xN₄** (**N₄**), **N₂S₂-OMe**, **N₂Se₂-OMe**, **N₂Te₂**, **N₂S₂-F**, **P₁**, **P₁-Bz_y**, **P₃**, and **P₃-Bz_y**, using 6–31G(d) basis sets; 3–21G** basis sets were used for **N₂Te₂**. Occupied MOs are denoted by small squares. The four key frontier π -MOs derived from the HOMO and LUMO of the $C_{16}H_{16}^{2-}$ parent hydrocarbon perimeter, which are used to calculate the Δ HOMO and Δ LUMO values in the context of Michl's perimeter model^[30] (Figure 4), are highlighted by thicker dark-gray lines, whilst lighter-gray lines are used to highlight MOs derived from the MOs of **P**, which were primarily associated with the inner perimeter of the π system (see the Supporting Information, Table S5). The “a” and “–a” MOs, which have nodal planes on the Group 16 heteroatoms ($1a_2$ and $1b_1^*$), are denoted by light-gray circles (Figure 3), whilst the “s” and “–s” MOs, which have significant MO coefficients ($1a_1$ and $1b_2^*$), are denoted by black triangles. MOs associated with the NMe₂ *para*-substituents of **N₂Se₂-NMe₂**, are offset to the right. The average HOMO–LUMO band gap values based on the energies of the “a”, “s”, “–a”, and “–s” MOs (small dark-gray diamonds) are plotted against a secondary ordinate. The trends observed in this data series closely mirror those in the observed (large light-gray diamonds) and calculated energies (small black diamonds) of the Q and B bands (bottom). Experimental values for the **N₂Y₂-OC₁₆H₃₃** compounds are plotted against the calculated values for their **N₂Y₂-OMe** counterparts.

There is no two-fold axis of symmetry in the optimized structures of **N₂Se₂** and **N₂Te₂**. One of the selenophene or tellurophene moieties tilts out of the saddled structure that is formed by the rest of the π system, due to a marked increase in the length of the C–Se and C–Te bonds. However, the two-fold axis of symmetry is retained in the X-ray structure of **N₂Se₂** and also when the structure is optimized by using the 3–21G** rather than the 6–31G(d) basis sets (Figure 1 and the Supporting Information, Figure S1).

Validation of the DFT and TD-DFT results by using MCD spectroscopy: The MO energies of the core-modified compounds can be readily compared to those of **P**, **TPP**, **TPTPhenP**, and the **2Phen_xN₄** model compound (Figure 8). Trends in the UV/Vis-absorption and MCD spectra can, in turn, be compared to the results of TD-DFT calculations and to changes in the Δ HOMO and Δ LUMO values (Figures 9–11 and the Supporting Information, Figures S5 and S6). The optical spectra of **N₂O₂**, **N₂S₂**, **N₂Se₂**, and **N₂Te₂** are broadly similar (Figure 9). A weaker set of bands at lower energy (600–1000 nm) and a more-intense set of bands at

higher energy (450–600 nm) can be readily assigned to Q and B transitions, respectively, on the basis of TD-DFT calculations (Table 2) and the presence of coupled pairs of *x*- and *y*-polarized and oppositely-signed \mathcal{B}_0 terms in the MCD spectra. Although the B band region of each spectrum is dominated by an intense close-lying pair of \mathcal{B}_0 terms (Figure 9 and Figure 11), the effects of incorporating fused phenanthrenes along the *y* axis on the energies of the weaker Q₀₀ bands would be very challenging in the absence of MCD data, due to the presence of relatively intense envelopes of vibrational bands (Figure 9). Widely separated and almost-forbidden \mathcal{B}_0 terms are also observed in the MCD spectra of **2Bz_x** and free-base **TPP** for the Q₀₀ bands, along with intense pseudo- \mathcal{A}_1 terms in the B band region.^[15] In both cases, their optical properties remain close to what would be anticipated for a *D*_{18h}-symmetric C₁₈H₁₈ parent perimeter and their major spectroscopic bands are broadly similar to the L and B bands of benzene.^[14] When Δ HOMO \approx Δ LUMO, the μ^+ contribution to the Q and B excited states is eliminated and the Q₀₀ bands remain forbidden because the ease of circulation of the excited electron

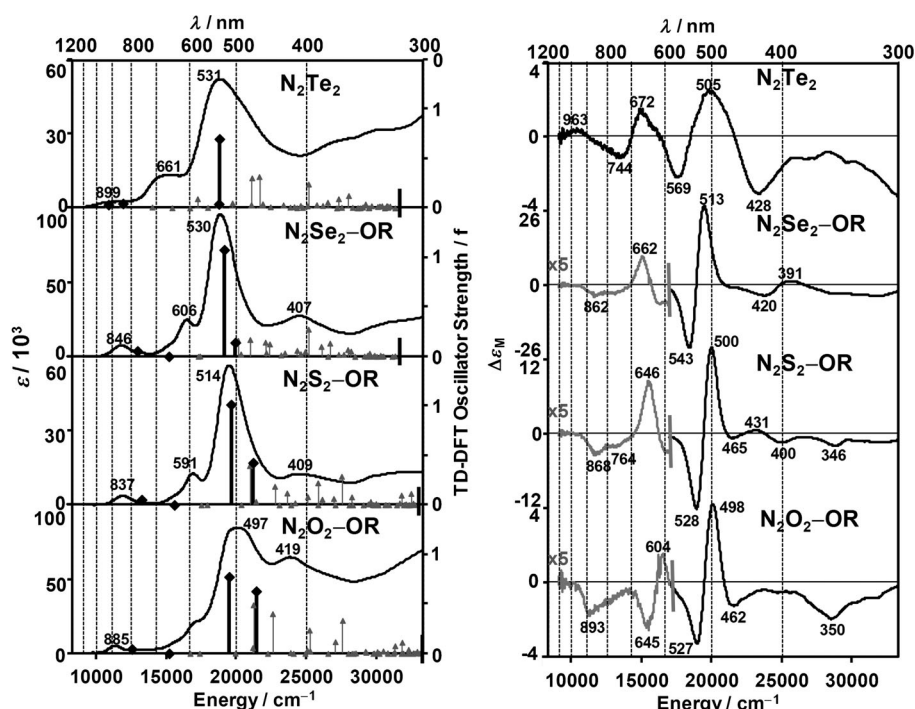


Figure 9. Observed electronic-absorption (left) and MCD spectra (right) of $\text{N}_2\text{O}_2\text{-OC}_{16}\text{H}_{33}$, $\text{N}_2\text{S}_2\text{-OC}_{16}\text{H}_{33}$, $\text{N}_2\text{Se}_2\text{-OC}_{16}\text{H}_{33}$, and N_2Te_2 , as well as their calculated TD-DFT (light-gray triangles) oscillator strengths (right axis) of N_2O_2 , N_2S_2 , N_2Se_2 , and N_2Te_2 . The Q and B bands, which are primarily associated with the four frontier π -MOs, are indicated by large dark-gray diamonds. For details of the most intense bands, see the Supporting Information, Table S4.

in the LUMO and that of the hole that is left in the HOMO are roughly comparable, as is the case in the parent hydrocarbon perimeter. The π systems of **2Bz_x** and free-base **TPP** are referred to as “soft MCD chromophores” in the context of Michl’s perimeter model because minor structural changes can reverse the alignment of the excited-state magnetic moments of the induced magnetic dipoles of the Q and B excited states and, hence, the observed sequence of signs in the MCD spectrum (Figure 10 and Figure 11).

Key trends in the optical properties of porphyrinoids can be rationalized by using Michl’s perimeter model, based on how different types of structural modification affect the relative magnitudes of the ΔHOMO and ΔLUMO (Figure 10). We recently demonstrated that sign sequences observed for the sequence of signs of the \mathcal{B}_0 terms that are associated with the Q and B bands of core-modified tetrabenzoporphyrinoids can be accurately predicted based on the ΔHOMO and ΔLUMO values derived from the MO energies predicted in B3LYP geometry optimizations and, moreover, that the sign sequences can be used to confirm the accuracy of the DFT description of the electronic structures.^[15] Replacing the protonated pyrrole groups at the 21 and 23 positions with a Group 16 heteroatom would not normally be expected to have a major effect on the OAM properties of the frontier π -MOs, because a lone pair of electrons in the p_z atomic orbital of one of the four core heteroatoms is directly replaced by another. Michl^[30] has demonstrated that the difference in electronegativity between the protonated

nitrogen atom and the heteroatom and the effect of changing the resonance integral between the heteroatom and the neighboring α -carbon atoms can modify the relative energies of the four frontier π -MOs to a limited extent. However, almost no difference is predicted between the ΔHOMO and ΔLUMO values of N_2O_2 , N_2S_2 , N_2Se_2 , and N_2Te_2 relative to the **2Phen_xN₄** model compound (Figure 10A), and similar trends are predicted when **TPP**, **2Bz_x**, **2Bz_y**, **TBP**, and **TPTBP** are core-modified with sulfur atoms (Figure 10B). As is the case with **2Bz_x**,^[15] B3LYP calculations predict that the ΔHOMO and ΔLUMO values of the core-modified diphenanthroporphyrins are relatively similar, but the reasons for this differ. In the context of the N_2Y_2 compounds, the “s” MO is the HOMO, due to the effect of ligand saddling on the level of

interaction between the phenyl groups and the *meso* carbon atoms. A much-larger destabilization of the “s” MO is predicted in the context of **TBP**, **TANP**, and **TPhenP** upon phenylation than for **P**, due to the steric hindrance between the π system and the *meso* substituents (Figure 10C). However, in the context of **P₃-Bz_y**, the “a” MO is the HOMO, due to the antibonding interaction between the π system of the porphyrin core and the peripheral C_4H_4 bridges (Figure 6). In this context, partial benzo substitution results in a stabilization of the “a” MO relative to **TBP** (Figure 8). The ΔHOMO values of the N_2Y_2 compounds decrease relative to **TPTPhenP** (Figure 10A) because there is a lower degree of saddling due to the removal of the two phenanthrenes that are aligned along the *y* axis, and this leads to a slight stabilization of the “s” MO (Figure 8). A significant ΔLUMO value is introduced in the context of the N_2Y_2 compounds when the stabilizing and destabilizing interactions with the “-s” and “-a” MOs along the *y* axis in the context of **TPTPhenP** are removed (Figure 6). With the exception of **P₃** and **N₂S₂-F**, in which $\Delta\text{HOMO} \approx \Delta\text{LUMO}$ (Figure 10A,D), and **N₂Te₂**, in which a marked deviation from the C_{2v} geometry is predicted (Figure 1), the sign sequences of the MCD bands predicted based on the B3LYP-optimized structures matches those observed experimentally (Table 2). Therefore, the DFT-based descriptions of the electronic structures (Table 2 and the Supporting Information, Table S5) are validated by the application of Michl’s perimeter model and the predicted trends can be used for the ra-

Table 2. Trends in the predicted MO energies [eV] in the TD-DFT calculations of **C₁₆H₁₆²⁺**, **P**, **TPP**, **TPhenP**, **TPTPhenP**, **2Phen_xN₄**, **N₂O₂**, **N₂O₂-OMe**, **N₂S₂**, **N₂S₂-OMe**, **N₂S₂-F**, **N₂Se₂**, **N₂Se₂-OMe**, **N₂Se₂-NMe₂**, **N₂Te₂**, **P₁-Bz_y**, and **P₃-Bz_y**, the *trans* and *cis* isomers of **P₁** and **P₃**, and the X-ray structures (X) of **P₃-Bz_y** and **N₂Se₂-NMe₂** (see the Supporting Information, Figure S1) and in the energies and signs of the Q bands based on B3LYP-geometry optimization and TD-DFT calculations with the 6-31G(d) basis sets unless otherwise stated.

	-s ^[a]		-a ^[a]		s ^[a]		a ^[a]		ΔL ^[b]	ΔH ^[b]	ΔL - ΔH ^[c]	Sign ^[d]	H-L ^[e]	av(H-L) ^[e]	Q _{obs} ^[f]	B _{obs} ^[f]	Sign _{obs} ^[g]
C₁₆H₁₆²⁺	1e _{4ux}	+5.87	1e _{4uy}	+5.87	1e _{5gx}	+2.80	1e _{5gy}	+2.80	0.00	0.00	0.00	-/+	3.07	3.07	-	-	-
P	1b _{3g} *	-2.22	1b _{2g} *	-2.23	1b _{1u}	-5.15	1a _u	-5.30	0.01	0.15	-0.14	-/+	2.92	3.00	2.01, 2.37	3.02, 3.14	-/+
TPP	2a*	-2.19	1a*	-2.20	1a	-4.91	2a	-5.20	0.01	0.29	-0.28	-/+	2.71	2.86	1.94, 2.29	2.95, 3.01	-/+
TPhenP	1b _{3g} *	-2.46	1b _{2g} *	-2.40	1b _{1u}	-5.18	1a _u	-4.98	-0.06	-0.20	-0.14	-/+	2.52	2.65	-	-	-
TPTPhenP	1b ₂ *	-2.58	1b ₁ *	-2.52	1a ₁	-4.47	1a ₂	-5.05	-0.06	0.58	-0.52	-/+	1.89	2.21	1.54, 1.60	2.12, 2.19	-/+
2Phen_xN₄	1b ₂ *	-2.55	1b ₁ *	-2.24	1a ₁	-4.70	1a ₂	-5.03	-0.31	0.33	-0.02	-/+	2.15	2.47	-	-	-
N₂O₂	1b ₂ *	-2.67	1b ₁ *	-2.34	1a ₁	-4.69	1a ₂	-5.02	-0.33	0.33	0.00	-/+	2.02	2.35	-	-	-
N₂O₂-OMe^[h]	1b ₂ *	-2.48	1b ₁ *	-2.12	1a ₁	-4.39	1a ₂	-4.85	-0.36	0.46	-0.10	-/+	2.02	2.31	1.39, 2.06	2.36, 2.50	-/+
N₂S₂	1b ₂ *	-2.70	1b ₁ *	-2.40	1a ₁	-4.78	1a ₂	-5.15	-0.30	0.37	-0.07	-/+	2.08	2.42	-	-	-
N₂S₂-OMe^[h]	1b ₂ *	-2.53	1b ₁ *	-2.19	1a ₁	-4.48	1a ₂	-4.98	-0.33	0.51	-0.18	-/+	1.95	2.37	1.43, 1.93	2.36, 2.49	-/+
N₂Se₂	1a'*	-2.75	1a***	-2.43	1a'	-4.78	1a''	-5.14	-0.32	0.36	-0.04	-/+	2.03	2.37	-	-	-
N₂Se₂-OMe^[h]	1b ₂ *	-2.54	1b ₁ *	-2.20	1a ₁	-4.47	1a ₂	-4.98	-0.34	0.51	-0.17	-/+	1.95	2.35	1.44, 1.88	2.29, 2.43	-/+
N₂Se₂-NMe₂	1b ₂ *	-2.25	1b ₁ *	-1.89	1a ₁	-4.03	1a ₂	-4.69	-0.36	0.63	-0.37	-/+	1.78	2.29	1.38, 1.80	2.23, 2.35	-/+
N₂Se₂-NMe₂ (X)	1b ₂ *	-2.58	1b ₁ *	-1.44	1a ₁	-3.92	1a ₂	-4.50	-1.14	0.58	0.56	+/-	1.34	2.22	1.38, 1.80	2.23, 2.35	-/+
N₂Te₂ (3-21G**)	1a'*	-2.86	1a***	-2.71	1a'	-4.71	1a''	-5.14	-0.15	0.43	-0.28	-/+	1.85	2.14	1.29, 1.85	2.19, 2.47	+/+
N₂S₂-F	1b ₂ *	-2.86	1b ₁ *	-2.57	1a ₁	-4.92	1a ₂	-5.31	-0.29	0.39	-0.10	-/+	2.06	2.40	1.55, 2.01	2.38, 2.52	+/-
P₁-trans	1a'*	-2.70	1a***	-2.56	1a'	-4.59	1a''	-5.21	-0.14	0.62	-0.48	-/+	1.89	2.27	1.46, 1.86	2.27, 2.39	-/+
P₁-cis-sp²	1b ₂ *	-2.68	1b ₁ *	-2.55	1a ₁	-4.58	1a ₂	-5.19	-0.13	0.61	-0.48	-/+	1.90	2.27	1.46, 1.86	2.27, 2.39	-/+
P₁-cis-sp³	1b ₂ *	-2.71	1b ₁ *	-2.57	1a ₁	-4.60	1a ₂	-5.22	-0.14	0.62	-0.48	-/+	1.89	2.27	1.46, 1.86	2.27, 2.39	-/+
P₁-Bz_y	1b ₂ *	-2.95	1b ₁ *	-2.42	1a ₁	-4.82	1a ₂	-5.03	-0.53	0.21	0.31	+/-	1.87	2.24	1.44, 1.75	2.30, 2.50	+/-
P₃-trans	1a'*	-2.71	1a***	-2.47	1a'	-4.84	1a''	-5.16	-0.24	0.32	-0.08	-/+	2.13	2.41	1.60, 1.75	2.45, 2.56	+/-
P₃-cis-sp²	1b ₂ *	-2.70	1b ₁ *	-2.46	1a ₁	-4.85	1a ₂	-5.15	-0.24	0.30	-0.06	-/+	2.15	2.42	1.60, 1.75	2.45, 2.56	+/-
P₃-cis-sp³	1b ₂ *	-2.72	1b ₁ *	-2.48	1a ₁	-4.83	1a ₂	-5.17	-0.24	0.34	-0.10	-/+	2.11	2.40	1.60, 1.75	2.45, 2.56	+/-
P₃-Bz_y	1b ₂ *	-2.96	1b ₁ *	-2.36	1a ₁	-5.10	1a ₂	-4.97	-0.60	-0.13	0.47	+/-	2.01	2.38	1.56, 1.67	2.35, 2.42	+/-
P₃-Bz_y (X)	2a*	-2.94	1a*	-2.31	1a	-5.17	2a	-4.98	-0.63	-0.19	0.44	+/-	2.04	2.45	1.56, 1.67	2.35, 2.42	+/-

[a] MO energies and symmetries of the four key frontier π-MOs derived from the HOMO and LUMO of the parent hydrocarbon perimeter. Michl's "a", "s", "-a", and "-s" terminology is used, based on the presence of nodal planes (a, -a) or large MO coefficients (s, -s) on the pyrrole nitrogen atoms on the y axis (Figure 3). [b] ΔLUMO (ΔL) and ΔHOMO (ΔH) values [eV], based on ΔH = s-a and ΔL = -s-a. [c] Difference between the ΔLUMO and ΔHOMO values (|ΔL| - |ΔH|). [d] The predicted MCD band sign sequences. [e] HOMO-LUMO band gap (H-L) and the average HOMO-LUMO band gap (av(H-L)), which takes into account all four frontier π-MOs, based on the TD-DFT calculations. [f] Average energies of the Q and B bands (Q_{obs}, B_{obs}), based on the energies of the coupled Faraday \mathcal{B}_0 terms in the MCD spectra. [g] Observed sequences of MCD signs, in ascending energy. [h] Observed values are for the corresponding 4-hexadecyloxy compounds.

tional design of ligands for use in practical applications. In contrast, predictions that are made based on the MO energies predicted by using ZINDO/s calculations are more problematic (see the Supporting Information, Table S6).

Effect of structural perturbation on the optical spectroscopy data: A key goal of recent porphyrinoid research has been to shift the Q band into the near-IR region, where it can be

better utilized in various applications. The key to achieving this shift is using different types of structural perturbation to narrow the HOMO-LUMO band gap, such as core modification with chalcogens, the inductive and mesomeric substituent effects of *para* substituents on the aryl groups, and the introduction of fused benzene rings along the y axis. The effect of forming diphenanthroporphyrins with fused-ring moieties that are oriented along the x axis must first be

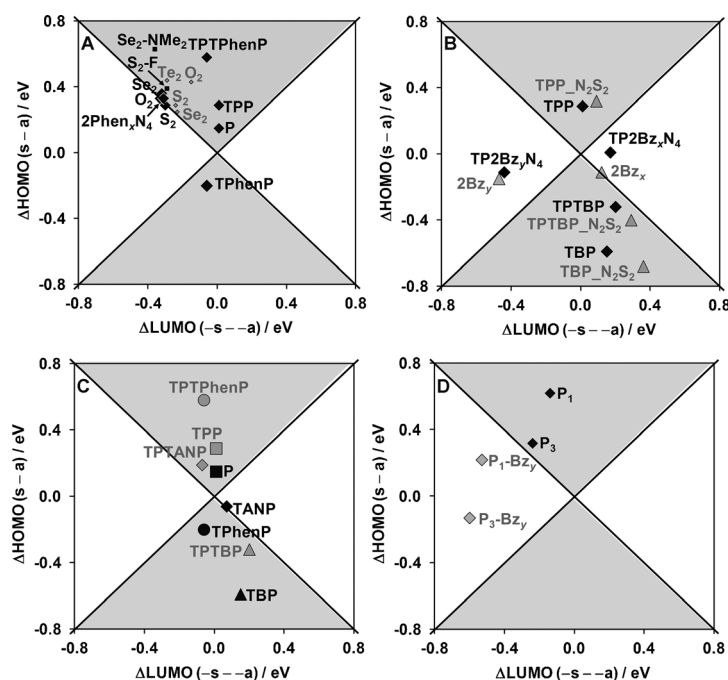


Figure 10. A) The effect of structural perturbation on the ΔHOMO and ΔLUMO values for N_2O_2 (O_2), N_2S_2 (S_2), $\text{N}_2\text{S}_2\text{-F}$ ($\text{S}_2\text{-F}$), N_2Se_2 (Se_2), $\text{N}_2\text{Se}_2\text{-NMe}_2$ ($\text{S}_2\text{-NMe}_2$), N_2Te_2 (Te_2), **P**, **TPP**, **TPhenP**, and **TPTPhenP**, as predicted by B3LYP-geometry optimizations; calculations that were carried out by using the 6-31G(d) and 3-21G** basis sets are denoted by black and gray diamonds, respectively. In the light-gray shaded areas, for which $\Delta\text{HOMO} > \Delta\text{LUMO}$, a $-/+$ MCD sign sequence is anticipated^[30] for the Q_{00} bands in ascending energy terms, whilst a $+/-$ sign sequence is anticipated in the unshaded areas, for which $\Delta\text{LUMO} > \Delta\text{HOMO}$. B) Plots of **TPP**, **TBP**, and **TPTBP**, their corresponding core-modified 21,23-dithiaporphyrinoid structures (**TPP-N₂S₂**, **TBP-N₂S₂**, and **TPTBP-N₂S₂**), **2Bz_x**, and **2Bz_y** (Figure 5), and their non-core-modified parent compounds (**TP2Bz_xN₄** and **TP2Bz_yN₄**), based on the B3LYP-optimized geometries with 6-31G(d) basis sets (top right). Black diamonds and gray squares are used to denote non-core-modified and core-modified compounds, respectively. C) Plots of **TBP**, **TPhenP**, **TANP**, and **P**, as well as their corresponding tetraphenyl compounds (**TPTBP**, **TPTPhenP**, **TPTANP**, and **TPP**), by using different sets of black and gray symbols, respectively. D) Plots of **P₁**, **P₁-Bz_y**, **P₃**, and **P₃-Bz_y** with black and gray symbols for the BCOD- and benzo-fused compounds, respectively.

taken into consideration. The “-s” MOs of **2Phen_xN₄** and **TPTPhenP** are predicted to have similar energies, whereas, in contrast, the “-a” MO of **2Phen_xN₄** is similar to that of **TPP**, because peripheral-fused phenanthrene rings are only present on the *x* axis (Figure 8). The decrease in ligand saddling (Table 1) results in a marked stabilization of the “s” MO relative to **TPTPhenP**. However, the energy of the “a” MO is largely unaffected by the removal of the two peripheral-fused phenanthrenes, because there is neither a bonding nor an antibonding interaction at the points where the fused rings are attached to the π system of the porphyrin core (Figure 6). If the π system were planar and did not contain any substituents on the *meso*-carbon atoms, the core-modified diphenanthroporphyrins would be expected to have an “s”, “a”, “-s”, “-a” ordering of the four frontier π -MOs, in ascending energy, similar to that of **TPhenP**, based on the stabilization of the “s” and “-s” MOs, due to large coeffi-

cients on the two heteroatoms that would replace the protonated pyrrole-nitrogen atoms (Figure 6 and the Supporting Information, Figure S3). The saddling of the ligand and the incorporation of aryl groups to form the **2Phen_xN₄** model compound results in an “a”, “s”, “-s”, “-a” ordering because there is a marked destabilization of the “s” MO, due to the large MO coefficients on the *meso*-carbon atoms (Figure 6 and the Supporting Information, Figure S3). This leads to a decrease in the average HOMO–LUMO band gap (Table 2), in which the energies of “a”, “s”, “-a”, and “-s” are all taken into consideration, because almost-equal contributions of one-electron transitions between all four frontier π -MOs contribute to the Q and B excited states of **TPP** in the context of Gouterman’s 4-orbital model^[31] (Table 2 and the Supporting Information, Figures S4 and S7).

Core modification to form N_2Y_2 structures: A further narrowing of the average HOMO–LUMO band gap is predicted upon core modification with chalcogens (Figure 8), primarily based on a slight relative destabilization of the “s” MO. Core modification results in a redshift of the lowest-energy Q and B bands on moving from **N₂S₂-OC₁₆H₃₃** to **N₂Se₂-OC₁₆H₃₃** and then to **N₂Te₂**, as well as on moving from **N₂S₂-OC₁₆H₃₃** to **N₂O₂-OC₁₆H₃₃**, which results in band centers that lie to the red side of the corresponding band in the spectrum of **TPTPhenP** (Figure 9). Although only relatively minor changes in the ΔHOMO and ΔLUMO values are predicted when Group 16 heteroatoms are incorporated along the *y* axis to form **N₂O₂**, **N₂S₂**, **N₂Se₂**, and **N₂Te₂** (Figure 10A), the absorption spectra of **N₂O₂** and **N₂Te₂** are markedly different from those of **N₂S₂** and **N₂Se₂** and the bands in the UV region increase in intensity relative to the Q and B bands. This increase is probably due to the effect of changes in the degree of saddling of the phenanthrene moieties and, where **N₂Te₂** is concerned, the effect on the vibrational bands of tilting one of the tellurophene moieties out of the saddled $\text{C}_{2v}(\sigma_{xz}, \sigma_{yz})$ symmetry structure (Figure 1 and Table 1). The Q_{00} bands of **N₂O₂**, **N₂S₂**, **N₂Se₂**, and **N₂Te₂** are relatively weak. The higher-energy Q_{00} bands appear as relatively intense positive \mathcal{B}_0 terms in the MCD spectrum at 600–700 nm. The band center of the MCD peak does not correspond with the main absorption band in this region of the spectrum, which is consistent with the B3LYP prediction that $\Delta\text{HOMO} \approx \Delta\text{LUMO}$ for these compounds (Figure 10A). When the Q_{00} bands are almost fully forbidden, vibrational bands tend to dominate the Q band region of the porphyrinoid spectra.^[14,31]

One clear drawback of making use of a **2Phen_x**-fused-ring substitution pattern is that the Q_{00} bands of **N₂O₂**, **N₂S₂**, **N₂Se₂**, and **N₂Te₂** have relatively weak intensities, because $\Delta\text{HOMO} \approx \Delta\text{LUMO}$, which could potentially limit the use of these compounds in applications that require strong absorbance in the NIR region. Therefore, further fine-tuning of their electronic properties could be desirable, with the key goals being to introduce a sufficient difference in the magnitude of the ΔHOMO and ΔLUMO values so that the

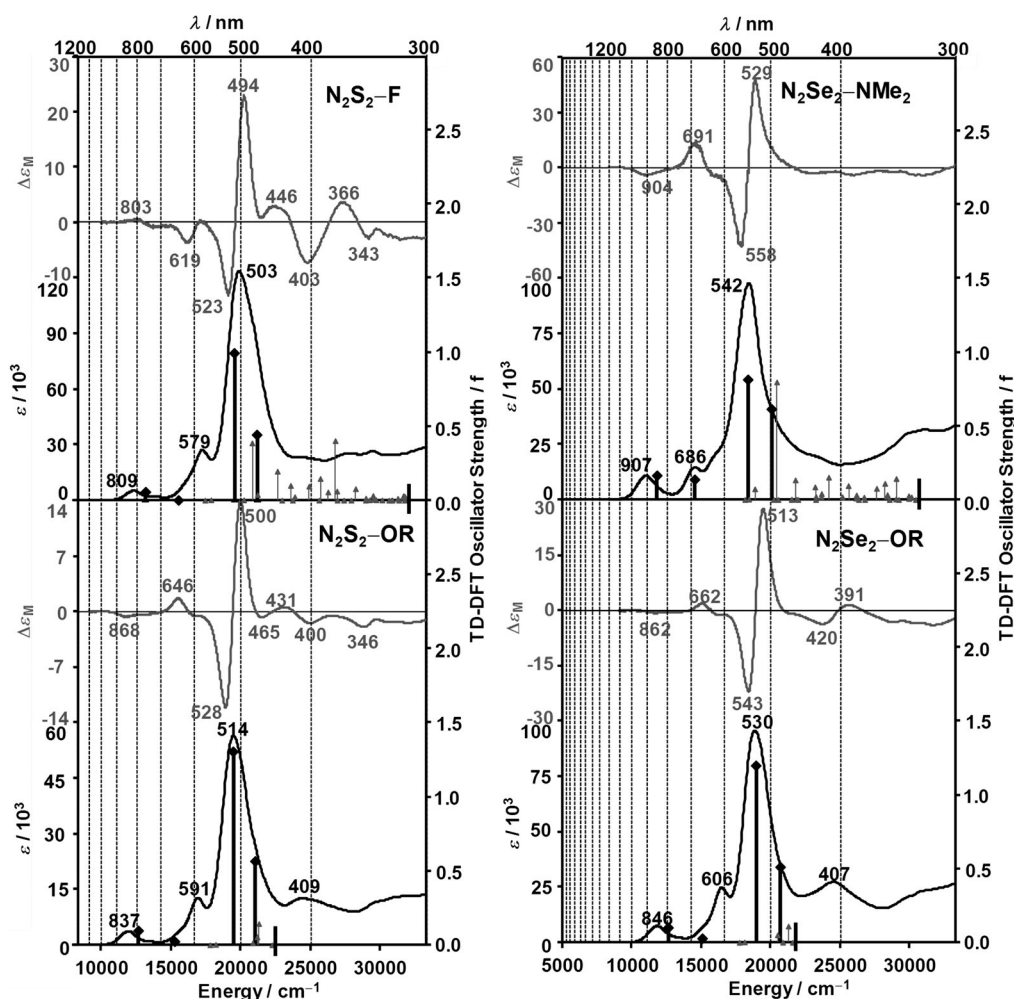


Figure 11. Observed electronic-absorption and MCD spectra of $\text{N}_2\text{S}_2\text{-OC}_{16}\text{H}_{33}$ and $\text{N}_2\text{S}_2\text{-F}$ (left), $\text{N}_2\text{Se}_2\text{-OC}_{16}\text{H}_{33}$ and $\text{N}_2\text{Se}_2\text{-NMe}_2$ (right), and their calculated TD-DFT oscillator strengths (light-gray triangles, right axis). Trace amounts of triethylamine were added to the solutions of $\text{N}_2\text{Se}_2\text{-NMe}_2$ and $\text{N}_2\text{S}_2\text{-F}$ to prevent protonation. The Q and B bands, which are primarily associated with the four frontier π -MOs, are indicated by large dark-gray diamonds. For details of the most intense bands, see the Supporting Information, Table S4.

allowed and forbidden properties of the Q and B bands mix substantially, whilst retaining a narrow HOMO–LUMO band gap and, hence, markedly redshifted Q_{00} bands. Two approaches have been explored in this regard: modifying the *para* substituents on the aryl groups at the *meso*-carbon positions, and the introduction of two fused benzene rings along the *y* axis. In this latter context, ABAB structures are formed with different types of fused rings along the *x* and *y* axes. The structures of P_1 and P_3 were selected because radially symmetric fused-ring expansion with acenaphthalene rings to form **TPTANP** is known to result in unusually large redshifts of the Q and B bands relative to **TPP**, in a similar manner to those observed with **TPTPhenP**.^[10a,b,16] The MO energies predict that this shift is due to a marked stabilization of the LUMO relative to the parent porphyrin and analogous benzo-fused compound (Figure 6). Because the nodal planes of the “–a” and “–s” MOs do not lie on alternating sets of atoms, unlike those of the “a” and “s” MOs (Figure 7), fused-ring expansion with different fused-ring systems can have different effects on the relative energies of

the four frontier π -MOs, depending on whether they are aligned with the *x* or *y* axes.

Inductive effects of the aryl substituents: It has long been known that an intensification and redshift of the Q_{00} bands of **TPPs** can be obtained by introducing substituents at the *para* positions of the *meso*-phenyl rings. In the 1970s, Kadish and Morrison^[32] demonstrated that the redox properties of **TPPs** with electron-withdrawing *para*-substituents could be adjusted in a predictable manner based on their Hammett parameter values (Table 3), due to changes in the energies of the HOMO and LUMO. We recently reported similar trends in the spectra of **TPTPhenPs** with F, Cl, Br, I, CH_3 , NO_2 , and $\text{N}(\text{CH}_3)_2$ groups at the *para* positions of the four *meso*-phenyl substituents.^[16] Similar trends are observed herein for the core-modified biphenanthroporphyrins. For example, a stabilization is predicted for the MO energies of $\text{N}_2\text{S}_2\text{-F}$ relative to N_2S_2 (Table 2), due to the electron-withdrawing effects of the halogen substituents. Michl demonstrated that the inductive effect of substituents should only

Table 3. Hammett parameter (σ_p) of the *para*-substituent,^[48] the first reduction (1st Red.) and the first and second oxidation (1st Ox., 2nd Ox.) potentials [V] relative to the saturated calomel electrode, and the gap between the first oxidation and reduction potentials ($\Delta E_{\text{ox-r}}$) of the compounds in CH_2Cl_2 .

	σ_p	1st Red. ^[a]	1st Ox. ^[a]	2nd Ox. ^[a]	$\Delta E_{\text{ox-r}}$ ^[b]	Q ^[c]
TPTPhenP	0.00	−0.93	0.90	—	1.83	1.57
N₂O₂-Br	0.23	−0.60	0.81	1.25	1.41	—
N₂O₂-I	0.18	−0.66	—	1.21	—	—
N₂O₂-Cl	0.23	−0.60	0.83	—	1.43	—
N₂O₂-F	0.06	−0.61	0.81	1.24	1.42	—
N₂O₂	0.00	−0.64	0.76	1.23	1.40	—
N₂O₂-OMe	−0.17	−0.68	0.67	1.03	1.35	1.39
N₂Se₂-OC₁₆H₃₃	−0.17 ^[d]	—	0.67	1.11	—	1.43
N₂Se₂-Cl	0.23	−0.54	0.99	1.34	1.53	—
N₂Se₂	0.00	−0.62	0.86	1.26	1.48	—
N₂Se₂-OC₁₆H₃₃	−0.17 ^[d]	−0.66	0.71	1.03	1.37	1.44
N₂Se₂-NMe₂	−0.83	—	0.34	—	—	1.38
N₂Te₂	0.00	−0.41	0.73	1.21	1.14	1.29
P₃	0.06	−0.77	0.95	1.39	1.72	1.60
P₃-Bz_y	0.06	−0.67	0.99	1.25	1.66	1.56

[a] Peak potentials were determined by differential pulse voltammetry (DPV). [b] Gap between the first oxidation and reduction potentials ($\Delta E_{\text{ox-r}}$) in eV. [c] Observed energies of the lowest-energy Q₀₀ bands, as identified by MCD spectroscopy in eV. [d] Hammett parameter for OCH₃ rather than OC₁₆H₃₃.

have a minor effect on the HOMO–LUMO band gap and, hence, on the optical properties, because the four frontier π -

MOs are stabilized or destabilized to approximately the same extent.^[30] Only minor shifts of the Q and B bands are observed in the spectra of **N₂S₂-OC₁₆H₃₃** and **N₂S₂-F**, as well as for the **N₂O₂-X** series (Figure 11 and Table 4), based on substitution with halogen atoms and weakly electron-donating alkoxy groups.

Mesomeric effects of the aryl substituents: As reported recently in the context of *para*-substituted **TPTPhenPs**,^[16] there is a strong mesomeric interaction between the NMe₂ substituents and the core of the π system when there is a severe saddling of the π system, because the phenyl rings are rotated into the plane of the inner-ligand perimeter due to steric crowding. The predicted MO energies for **N₂Se₂** and **N₂Se₂-NMe₂** (Figure 3) demonstrate that the incorporation of strongly electron-donating NMe₂ groups has a more significant effect on the relative energies of the key frontier π -MOs on the inner-ligand perimeter than the inductive effects that are introduced by halogen atoms. Marked changes in the wavelengths and intensities of the Q and B bands of **N₂Se₂-NMe₂** and **N₂Se₂-OC₁₆H₃₃** compounds are observed (Figure 10A, Figure 11, and Table 4). In contrast with the Q bands of **N₂S₂-F**, which are almost fully forbidden because $\Delta\text{HOMO} \approx \Delta\text{LUMO}$ (Figure 11 and Table 2), there is a significant intensification of the Q band region of **N₂Se₂-NMe₂**, due to a mixing of the forbidden and allowed properties of

Table 4. Absorption and emission data for **N₂O₂**, **N₂S₂**, **N₂Se₂**, **N₂Te₂**, and **TPTPhenP**, **P₁-Bz_y**, **P₁**, **N₂Se₂-OMe**, **N₂Se₂-NMe₂**, and **N₂O₂-X** (X = halogen) in their free-base and protonated forms^[a] ($c = 1 \mu\text{M}$ in CHCl_3 , 298 K).

	B bands	λ_{abs} [nm] ($\log \epsilon^{[b]}/\text{M}^{-1} \text{cm}^{-1}$)	Q bands	λ_{em} [nm]	$\Delta \tilde{\nu}_{\text{abs-em}}$ [cm^{-1}]	Φ_f $\times 10^3$	τ_f [ps]	k_f [$\times 10^7 \text{s}^{-1}$]	k_{nr} [$\times 10^9 \text{s}^{-1}$]
N₂O₂	497 (4.92)		842 (3.73)	906	840	1.0	276	0.3	3.6
N₂O₂H₂²⁺	507 (4.98), 539 (4.87)		802 (4.15)	861	850	3.2	169	1.9	5.9
N₂S₂	504 (4.75)		812 (3.35)	908	1300	0.87	130	0.7	7.7
N₂S₂H₂²⁺	530 (4.67), 575 (4.70)		859 (3.95)	933	920	0.97	69	1.4	14.5
N₂Se₂	521 (4.98)		820 (3.65)	911	1220	0.12	25	0.5	40.0
N₂Se₂H₂²⁺	536 (4.80), 584 (4.88)		858 (4.25)	922	810	(0.07) ^[e]	11	(0.6) ^[e]	(83) ^[e]
N₂Te₂	531 (4.72)		918 (3.34)	—	—	< 0.05	< 3	—	—
N₂Te₂H₂²⁺	532 (4.77), 594 (4.89)		900 (4.29)	—	—	< 0.05	< 3	—	—
TPTPhenP^[b]	576 (4.92)		794 (4.14)	831	560	5.7	380	1.5	2.6
TPTPhenPH₂²⁺[b]	579 (5.04)		803 (4.21)	838	520	8.0	420	1.9	2.4
P₁	533 (5.18)		861 (4.04)	942	1010	0.40	61	0.7	16.4
P₁H₂²⁺	542 (5.08), 572 (5.08)		735 (4.65), 849 (4.54)	918	880	1.1	68	1.6	14.7
P₁-Bz_y	543 (5.32)		712 (4.72), 866 (4.16)	986	1350	0.27	54	0.5	18.5
P₁-Bz_yH₂²⁺	551 (5.31), 595 (5.43)		688 (4.60), 760 (4.46), 896 (4.71)	966	810	0.62	57	1.1	17.5
N₂Se₂-NMe₂	543 (4.99)		910 (4.08)	—	—	< 0.1	24	—	—
N₂Se₂-NMe₂H_n⁺⁺	591		875, 1140	—	—	< 0.05	< 3	—	—
N₂Se₂-OMe	529 (5.04)		843 (3.90)	940	1220	(0.05) ^[e]	20	(0.3) ^[e]	(50) ^[e]
N₂Se₂-OMeH₂²⁺	548 (4.89), 596 (4.85)		763 (4.47), 934 (4.45)	(1025) ^[d]	(900) ^[d]	< 0.05 ^[d]	— ^[d]	— ^[d]	— ^[d]
N₂O₂-F	497 (4.80)		851 (3.68)	915	820	0.70	306	0.2	3.3
N₂O₂-FH₂²⁺	509 (4.94)		804 (4.12)	865	880	3.1	174	1.8	5.7
N₂O₂-Cl	499 (4.82)		854 (3.52)	913	760	1.0	219	0.5	4.6
N₂O₂-CH₂²⁺	519 (4.90)		809 (4.10)	873	910	2.1	118	1.8	8.5
N₂O₂-Br	499 (4.91)		853 (3.62)	913	770	0.95	195	0.5	4.6
N₂O₂-BrH₂²⁺	519 (4.96)		808 (4.15)	874	930	1.9	99	1.9	8.5
N₂O₂-I	502 (4.63) ^[e]		856 (3.51) ^[e]	913	730	— ^[f]	117	— ^[f]	— ^[f]
N₂O₂-IH₂²⁺	525 (4.78) ^[e]		814 (4.00) ^[e]	884	970	0.84	54	1.6	18.5

[a] Protonation was carried out by adding 1 % TFA (v/v) to the solution of the corresponding porphyrin in CHCl_3 . [b] Taken from reference [16], except for the lifetimes of the protonated species, which were determined herein. [c] Higher uncertainty for ϵ (20 %) because of low solubility. [d] The fluorescence band was too redshifted and too weak to be reliably determined. [e] High uncertainty of Φ_f (> 30 %) and high uncertainty of the photophysical data due to weak fluorescence. [f] Could not be reliably determined because the compound decomposed in its free-base form over the long measurement time that was required to record the weak, redshifted fluorescence.

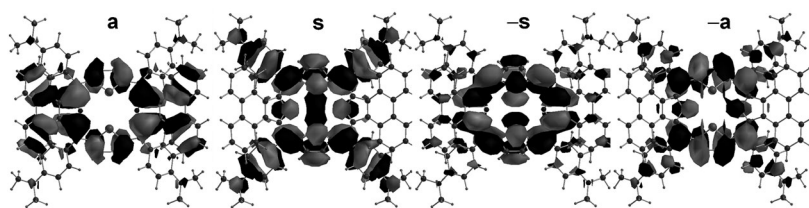


Figure 12. Nodal patterns of the four frontier π -MOs of $\text{N}_2\text{Se}_2\text{-NMe}_2$ at an isosurface value of 0.015, which demonstrate that the largest interactions between the aryl substituents and the four frontier π -MOs are predicted in the context of the “s” MO.

the Q and B bands. The observed spectroscopic properties can be readily explained in qualitative terms using Michl’s perimeter model based on the ΔHOMO and ΔLUMO values predicted for the B3LYP-optimized geometry. Marked differences in the ΔHOMO and ΔLUMO values are anticipated because the NMe_2 groups will have differing effects based on the size of the MO coefficients at the *para* positions of the phenyl rings and at the *meso*-carbon atoms. The largest effect is anticipated for either the “a” or “s” MO, based on mixing with close-lying occupied NMe_2 MOs of the same symmetry (Figure 8). Michl’s perimeter model can be used to demonstrate that a greater destabilization is expected for the “s” MO because there are large MO coefficients rather than nodal planes on the *meso*-carbon atoms at which the aryl groups are attached (Figure 12). Because $\Delta\text{HOMO} \approx \Delta\text{LUMO}$ in the case of N_2Se_2 , this destabilization should lead to a larger ΔHOMO value, as is predicted for the B3LYP-optimized geometry (Table 2). Therefore, a $-/+/-/+$ sequence in the Faraday \mathcal{B}_0 terms is anticipated with ascending energy, as observed experimentally (Figure 11), along with an intensification of the Q_{00} bands, due to the mixing of the forbidden and allowed properties of the Q and B transitions that occurs when $\Delta\text{HOMO} > \Delta\text{LUMO}$. However, the destabilization of the frontier π -MOs leads to a marked decrease in the first oxidation potential (Table 3), which could lead to issues with stability that could potentially complicate their use in future applications. Ideally, the narrowing of the HOMO–LUMO band gap would be achieved by a stabilization of the LUMO rather than by a destabilization of the HOMO.

ABAB-fused-ring expansion: The second approach that was explored to enhance the intensity of the Q band region was the incorporation of benzo groups along the y axis by using a BCOD-fused-thiophene precursor. The BCOD moieties of P_1 and P_3 (Figure 1) were then converted into $\text{P}_1\text{-Bz}_y$ and $\text{P}_3\text{-Bz}_y$ compounds with fused-benzene rings based on a retro-Diels–Alder reaction.^[15] Although the incorporation of F substituents at the *para* positions of the phenyl groups results in slight blueshifts of the Q and B bands, a potential advantage is that the stabilization of the frontier π -MOs makes these compounds more stable towards oxidative attack (Table 3). Figure 6 demonstrates that the introduction of either acenaphtho- or phenanthro-fused-ring moieties along the x axis can be expected to result in a marked stabilization of the “–s” MO, due to the strong bonding interac-

tions between the fused-ring moieties and the core porphyrin ligand at the points of attachment. This interaction is absent in the context of the “–a” MO of the N_2Y_2 -core-modified biphenanthroporphyrins, because it would be aligned with the y axis, which is unsubstituted in this context (Figure 1). This explains why

the “–s” MO is consistently the LUMO in the context of the N_2Y_2 compounds (Figure 8). An examination of the nodal patterns of the four frontier π -MOs of **TBP** (Figure 6) makes it clear that benzo substitution along the y axis can be expected to stabilize the “s” and “–s” MOs and destabilize the “a” and “–a” MOs, based on whether there is a bonding or antibonding interaction at the β -pyrrole carbon atoms to which the benzo moieties are fused. The extra stabilization of the “–s” MO results in a significant increase in the ΔLUMO values of $\text{P}_1\text{-Bz}_y$ and $\text{P}_3\text{-Bz}_y$ relative to those of P_1 and P_3 (Figure 13). The stabilization of the “s” MO and destabilization of the “a” MO results in a lower ΔHOMO value and a HOMO that lies at an energy comparable to that of **TPP** (Figure 8), which results in a reversal of the observed MCD-sign sequence of the Q and B bands of $\text{P}_1\text{-Bz}_y$ and $\text{P}_3\text{-Bz}_y$ (Figure 13) and an intensification of the Q bands, because there is a mixing of the forbidden and allowed properties of the Q and B bands when $\Delta\text{LUMO} > \Delta\text{HOMO}$. The redox properties of $\text{P}_1\text{-Bz}_y$ and $\text{P}_3\text{-Bz}_y$ could enhance the utility of these compounds in many applications. Although the lower-energy Q band of $\text{P}_1\text{-Bz}_y$ at 869 nm is significantly redshifted compared with the corresponding band of **TPTPhenP** (809 nm), there is a marked stabilization of the HOMO (the “s” MO of $\text{P}_1\text{-Bz}_y$ and the “a” MO of $\text{P}_3\text{-Bz}_y$) relative to that of **TPTPhenP**, which leads to an increase (rather than a decrease) in the first oxidation potential (Table 3). In marked contrast with the introduction of NMe_2 substituents onto the aryl groups of $\text{N}_2\text{Se}_2\text{-NMe}_2$, the narrowing of the HOMO–LUMO band gap is primarily achieved through a significant stabilization of the LUMO, rather than through a further destabilization of the HOMO, owing to the stabilizing effects of the fused rings along both the x and y axes.

Marked differences are observed between the spectra of P_1 and P_3 , based on whether phenanthro- and acenaphtho-fused rings are present along the x axis, respectively. A significantly larger ΔHOMO value is predicted for P_1 relative to P_3 (Figure 10D), due to a larger destabilization of the “s” MO (Figure 8, Table 2), based on a greater folding of the π system (Table 1), due to the greater steric hindrance between the phenyl groups and the larger phenanthrene-fused rings. As a result, the B3LYP calculations predict that $\Delta\text{HOMO} > \Delta\text{LUMO}$ for P_1 , whilst P_3 is a soft MCD chromophore with $\Delta\text{HOMO} \approx \Delta\text{LUMO}$ (Figure 10D). This difference is reflected in the close alignment between the intense coupled oppositely signed x- and y-polarized \mathcal{B}_0 terms

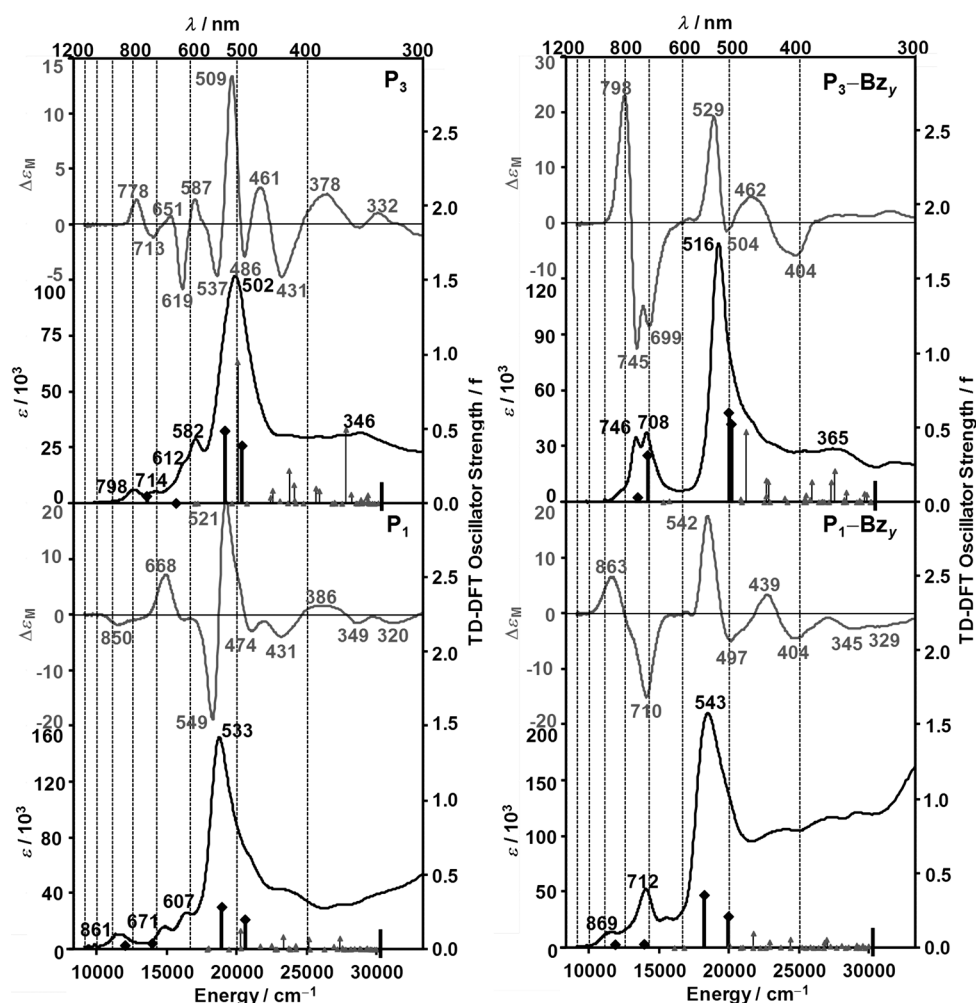


Figure 13. Observed electronic-absorption and MCD spectra of **P**₁ and **P**₃ (left), **P**₁-Bz_y and **P**₃-Bz_y (right), and their calculated TD-DFT oscillator strengths (light-gray triangles, right axis). Trace amounts of triethylamine were added to prevent protonation. The Q and B bands, which are primarily associated with the four frontier π -MOs, are indicated by large dark-gray diamonds. For details of the most intense bands, see the Supporting Information, Table S4.

at 850, 668, 549, and 521 nm in the MCD spectrum of **P**₁ and their corresponding bands in the absorption spectrum, whilst a much more complex spectrum is predicted for **P**₃ (Figure 13). When the Q₀₀ bands are almost fully forbidden, most of the intensity in the near-IR region is derived from vibrational borrowing from the allowed B₀₀ bands.^[14,31] For this reason, the assignment of the higher-energy Q₀₀ band of **P**₃ is problematic. There is a slight blueshift of the Q₀₀ and B₀₀ bands of **P**₃ and **P**₃-Bz_y relative to the corresponding bands in the spectra of **P**₁ and **P**₁-Bz_y, due to a narrowing of the average HOMO–LUMO band gap (Figure 8 and Table 2). This is primarily due to the greater destabilization of the “s” MO (Figure 8 and Table 2). It should be noted that the calculated MO energies and the calculated TD-DFT and ZINDO/s spectra of the *cis* and *trans* isomers of **P**₁ and **P**₃, with respect to the BCOD substituents, were very similar to their corresponding data for the *trans* isomers (Figure 3, Table 2, and the Supporting Information, Fig-

ures S6 and S12, and Tables S4 and S7); thus, structural isomerism of **P**₁ and **P**₃, based on the relative orientation of the fused BCOD moieties, is not expected to play a major role in determining the optical properties.

Accuracy of the TD-DFT calculations: In many instances, the TD-DFT calculations appear to predict the presence of more intense bands in the B band region than are actually observed. Similar issues have previously been reported for a wide range of porphyrinoids.^[14] Two intense *xy*-polarized electronic bands tend to be predicted in the B band region of ZnP based on TD-DFT calculations,^[29a] whilst only one is observed experimentally.^[14] ZINDO/s calculations (see the Supporting Information, Figures S9–S13 and Table S7) tend to consistently predict a single intense pair of *x*- and *y*-polarized B bands. The additional predicted bands appear to be associated with a systematic overestimation of the level of configurational interaction between the B and higher-energy $\pi\pi^*$ states.^[14] Reimers and co-workers^[33] recently demonstrated that calculations that were carried out with the BP86 and

B3LYP functionals underestimated the energy of states that was associated with the $1b_{2u} \rightarrow 1e_g^*$ one-electron transition of free-base porphyrins and their fused-ring-expanded analogues, due to their charge-transfer character, and that a larger Hartree–Fock component was required to compensate for this. This issue has not been pursued in depth in the context of this study because our primary goal has been to account for the observed trends in the properties in the Q band region based on the energies of the four “Gouterman orbitals”.

Effect of protonation: The optical properties of porphyrinoids can also be modulated by protonating the pyrrole-nitrogen atoms on the inner perimeter of the π system to form a dicationic species.^[10b,16,31] The observed trends for the various Group-16-substituted compounds (Table 4 and Figure 14) mirrored those described above in the context of Figure 9. The Q bands of **N**₂S₂, **N**₂Se₂, and **TPTPhenP**^[16] are

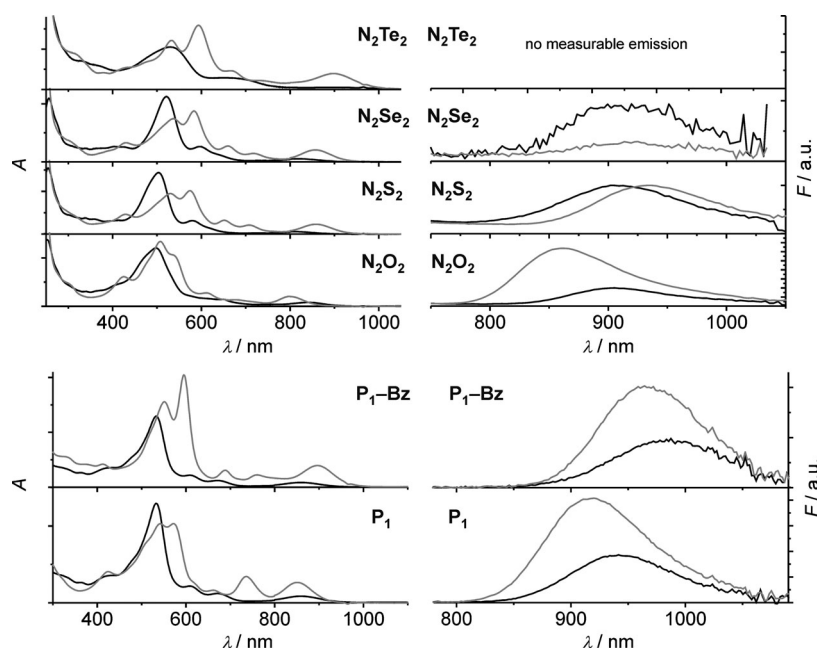


Figure 14. Absorption (left) and emission spectra (right) of N_2O_2 , N_2S_2 , N_2Se_2 , and N_2Te_2 (top), as well as P_1 and $\text{P}_1\text{-Bz}_y$ (bottom) in CHCl_3 (black) and after the addition of 1% TFA (v/v; gray).

markedly redshifted and become more intense upon protonation, but a blueshift is observed in the spectra of N_2O_2 and N_2Te_2 compounds. A redshift and splitting of the B bands is consistently observed. Similar minor differences are observed in the spectra of P_1 and $\text{P}_1\text{-Bz}_y$ (Table 4). Protonation of P_1 results in a blueshift of the lowest-energy Q band, but a redshift in the spectrum of $\text{P}_1\text{-Bz}_y\text{H}_2^{2+}$ (Figure 14). Protonation further enhances the marked redshifts, due to core modification and *para*-phenyl substitution. The lowest-energy Q_{00} band is at 900 nm for $\text{N}_2\text{Te}_2\text{H}_2^{2+}$ and at 1140 nm for $\text{N}_2\text{Se}_2\text{-NMe}_2\text{H}_n^{n+}$ (Table 4 and Figure 14).^[34] Upon protonation, there is a redshift of the lowest-energy Q_{00} band and a complex series of spectra that are based on protonation at the ligand core and at the *p*- NMe_2 substituents, similar to those reported for the analogous TPTPhenPH_2^{2+} species.^[16] In the UV region, the electronic-absorption spectra are comprised of a relatively intense envelope of extensively overlapping bands (Figure 9, Figure 11, and Figure 13). These bands can be assigned to transitions that involve MOs that are primarily associated with the peripheral fused rings, because weak MCD intensity would be anticipated relative to bands that are primarily associated with the “a” and “s” MOs on the inner-ligand perimeter due to the weaker OAM properties.

Fluorescence spectroscopy: The impact of core modification with Group 16 heteroatoms on fluorescence properties has also been studied. In general, a redshift of the S_1 emission band is observed, along with a decrease in the fluorescence quantum yield (Φ_f , Table 4). The emission bands of N_2O_2 and N_2S_2 are centered at $\lambda > 900$ nm, with fluorescence quantum yields of about 0.1% in CHCl_3 . The Φ_f value increases three-fold upon the protonation of N_2O_2 to form

$\text{N}_2\text{O}_2\text{H}_2^{2+}$, whilst the emission band is blueshifted (from 906 to 861 nm), thereby resulting in a virtually unchanged Stokes shift of about 850 cm^{-1} . However, the increase in fluorescence intensity is less pronounced in the case of $\text{N}_2\text{S}_2\text{H}_2^{2+}$ relative to N_2S_2 and the fluorescence maximum is redshifted in a similar manner to the Q_{00} absorption-band maxima. The relatively narrow Stokes shifts in the spectra of N_2O_2 and $\text{N}_2\text{O}_2\text{H}_2^{2+}$, the decrease in the Stokes shift upon protonation of N_2S_2 , and the increase in the radiative rate constant (k_f) for both protonated species suggest that there is a more rigid saddling distortion of the ligand upon protonation of the core pyrrole-nitrogen atoms and a loss of conformational flexibility.

Further decreases in emission intensity are observed for the selenophene- and, especially, the tellurophene-containing compounds. All of the fluorescence-decay curves are monoexponential and display fluorescence lifetimes of $\tau_f > 300$ ps. Table 4 also reveals that nonradiative processes are accelerated in the series N_2Y_2 , with $\text{Y} = \text{O} \rightarrow \text{S} \rightarrow \text{Se} (\rightarrow \text{Te})$, due to a gradual increase in k_{nr} . Because the emission maxima remain relatively constant for the furan, thiophene, and selenophene derivatives (906, 908, and about 910 nm, respectively, Table 4), the decrease in emissivity can be attributed to the increasing influence of the heavy-atom effect. The “energy-gap rule”^[35] clearly only plays a minor role, so it is safe to assume that the difference in fluorescence intensity is only due to enhanced nonradiative deactivation through intersystem crossing and that $k_{nr} \approx k_{isc}$. Therefore, the heavy-atom effect can be quantified by using a central-field single-electron approximation for the relationship between k_{isc} and the spin-orbit coupling constant.^[36] An excellent correlation is obtained for both N_2Y_2 and $\text{N}_2\text{Y}_2\text{H}_2^{2+}$ when $\log k_{nr} + \log n^6$ (n = quantum number) is used as a measure of the heavy-atom effect (Figure 15). An enhancement of the spin-orbit coupling and, hence, intersystem crossing, affords a novel set of porphyrinoids, which could potentially be used in applications that require singlet-oxygen generation. Usually, such sensitizers contain bromo or iodo atoms as heavy-atom substituents. An obvious question in this regard is whether core substitution with chalcogens or the conventional halogen substitution at the periphery provides the best Φ_A values. Data obtained for $\text{N}_2\text{O}_2\text{-X}$ in both the free-base and doubly protonated forms were analyzed, as was data that were previously recorded for the corresponding *para*- X -*meso*-phenyl-substituted TPTPhenPs .^[16] The plots, shown in Figure 15, confirm that acceptable correla-

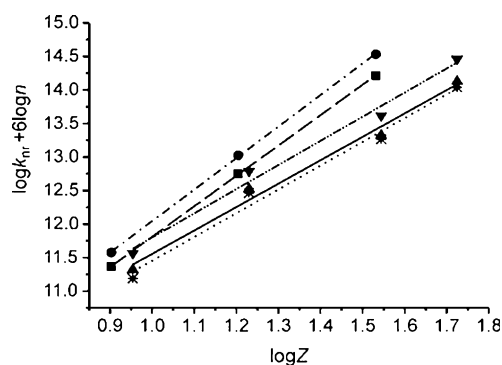


Figure 15. Plot of the heavy-atom-quenching effect on the fluorescence of the porphyrin; symbols denote the data and lines denote linear fits that were calculated based on $y = mx + b$, in which m = slope and b = intercept. ■ and ---: the N_2O_2 , N_2S_2 , and N_2Se_2 series ($m = 4.53$, correlation coefficient $r^2 = 0.999$); ● and - - - -: the $\text{N}_2\text{O}_2\text{H}_2^{2+}$, $\text{N}_2\text{S}_2\text{H}_2^{2+}$, and $\text{N}_2\text{Se}_2\text{H}_2^{2+}$ series ($m = 4.70$, $r^2 = 0.999$); ▲ and —: the $\text{N}_2\text{O}_2\text{-X}$ series ($\text{X} = \text{F, Cl, Br, I}$; $m = 3.49$, $r^2 = 0.988$); ▼ and ——— line: the $\text{N}_2\text{O}_2\text{-XH}_2^{2+}$ series ($m = 3.60$, $r^2 = 0.988$); * and ·····: **TPTPhenP** derivatives that contained the same X substitution pattern on the *meso*-phenyl rings as the $\text{N}_2\text{O}_2\text{-X}$ series ($m = 3.55$, $r^2 = 0.986$; data taken from ref. [16]).

tions are also obtained for the peripherally substituted compounds. A comparison of the slopes of these fits suggests that core modification accelerates intersystem crossing to a greater extent than peripheral substitution, because $m_{\text{core}} \approx 4.6$ compared to $m_{\text{periphery}} = 3.5$.

Performance as photosensitizers: Because the core-modified porphyrinoids reported herein have Q or B bands that lie in the biomedical NIR window and exhibit pronounced heavy-atom-quenching properties, their potential suitability as photosensitizers for possible applications in photodynamic therapy has also been explored. N_2Se_2 , N_2Te_2 , and $\text{N}_2\text{O}_2\text{-I}$ are especially interesting in this regard, because high intersystem-crossing yields are a prerequisite for high quantum yields of singlet-oxygen production (Φ_Δ). Therefore, N_2O_2 , N_2Se_2 , N_2Te_2 , and $\text{N}_2\text{O}_2\text{-I}$ were tested according to the following procedure: A solution of the porphyrinoid photosensitizer (absorbance = 0.52 at 515 nm, $c = 5 \mu\text{M}$) and 1,3-diphenylisobenzofuran (DPBF, 50 μM) was prepared in DMF and inserted into a quartz cuvette. DPBF is an optical indicator for $^1\text{O}_2$ generation because an endoperoxide is formed upon cycloaddition with singlet oxygen, thereby resulting in the disappearance of its characteristic absorption band at 415 nm.^[37] The solutions were irradiated at 515 nm (in the B band region of the porphyrins) for 30 min (Xe lamp 25.4 A) and absorption spectra were recorded at 5 min intervals (see the Supporting Information, Figure S14). A solution of **TPP** in DMF was used as the standard for the calculation of Φ_Δ ($\Phi_\Delta^{\text{TPP}} = 0.67$).^[38] Unfortunately, with the exception of N_2Se_2 , the porphyrins tested herein either induced no change in the DPBF absorption (N_2O_2 and N_2Te_2) or decomposed upon irradiation ($\text{N}_2\text{O}_2\text{-I}$). A Φ_Δ value of 0.13 for N_2Se_2 was calculated from the slope of the decrease in absorption intensity by using Equation (4),^[39] in which m de-

notes the slopes of the decrease in the absorption of DPBF at 415 nm for N_2Se_2 and **TPP** (in min^{-1}).

$$\Phi_\Delta(\text{N}_2\text{Se}_2) = \Phi_\Delta(\text{TPP}) \times m(\text{N}_2\text{Se}_2) \times m(\text{TPP})^{-1} \quad (4)$$

Although the yield of $^1\text{O}_2$ is only moderate in comparison to that from **TPP**, the possibility of using irradiation at wavelengths above 800 nm might provide advantages. Expanded tests are planned as part of our future work in this area.

Conclusion

A wide range of core modified diphenanthroporphyrins have been prepared, in which the protonated pyrrole nitrogen atoms are replaced by Group 16 heteroatoms, to explore trends in the optical properties and electronic structures and to study the suitability of these compounds for near IR region dye applications. The goal was to prepare compounds with optical properties similar to those of tetraphenyltetraphenanthroporphyrins, which have the most redshifted Q and B bands for a fused-ring-expanded analogue of **TPP**,^[16] but with less severely saddled structures. An application of Michl's perimeter model to the MCD spectra broadly validates the DFT based descriptions of the electronic structures and provides a readily accessible conceptual framework for identifying the key structure-property relationships in a manner which can potentially enable the rational design of novel porphyrinoids suitable for use in specific applications. The optical spectra of N_2O_2 , N_2S_2 , N_2Se_2 and N_2Te_2 compounds are broadly similar, since in each instance the heteroatom provides a lone pair to the π -system as would be the case with the protonated pyrrole nitrogen atoms in the parent diphenanthroporphyrin compound, but the spectra of the $\text{N}_2\text{O}_2\text{-OC}_{16}\text{H}_{33}$ and N_2Te_2 compounds differ markedly from their $\text{N}_2\text{S}_2\text{-OC}_{16}\text{H}_{33}$ and $\text{N}_2\text{Se}_2\text{-OC}_{16}\text{H}_{33}$ counterparts due to changes in the degree of ligand saddling. Although the Q band of N_2Te_2 is markedly redshifted relative to **TPTPhenP** for this reason, the compound is unstable to oxidation due to the destabilization of the HOMO and is not likely to be useful for optoelectronic or photodynamic applications. The effect of other structural modifications, such as the introduction of different *meso*-aryl groups and expansion of the inner perimeter of the ligand by incorporating two additional Group 16 heteroatoms and modifications to the fused-ring-expansion pattern, to further fine-tune the optical properties was explored. Incorporation of electron donating -NMe_2 groups at the *para*-positions introduces a strong mesomeric interaction with the main porphyrin macrocycle which results in a significant intensification and redshift of the Q bands. A marked decrease in the first oxidation potential due to a destabilization of the LUMO is potentially problematic, however. The use of BCOD-fused thiophene precursors enables the synthesis of diphenanthro- and diacenaphtho-fused N_2S_2 compounds with ABAB structures containing two benzo-fused thio-

phene moieties. These compounds exhibit a narrowing of the HOMO–LUMO band gap relative to **TPP** due primarily to a stabilization of the LUMO rather than a destabilization of the HOMO and enhanced absorption intensity in the NIR region due to a significant increase in the Δ LUMO value. An analysis using Michl's perimeter model demonstrates that the differing effects of incorporating benzene, phenanthrene and acenaphthalene fused ring moieties along the *x* and *y*-axes to form ABAB structures can substantially modify the relative energies of the four frontier π -MOs. Some of the core modified diphenanthroporphyrins studied are promising candidates for use in photodynamic therapy. A fluorescence emission study was carried out which demonstrates that core modification has a stronger influence on heavy atom quenching than the introduction of peripheral substituents such as -Br and -I.

Experimental Section

General: ^1H and ^{13}C NMR spectra were acquired at 500 MHz and 125 MHz on a Bruker DRX500 spectrometer. NMR chemical shifts are expressed relative to TMS as an internal standard. MS (MALDI-TOF) was performed on an ABI Voyager De pro spectrometer. Elemental analysis was performed on a Perkin–Elmer 240 C elemental analyzer. Melting points were determined by using a Reichert Thermometer and are without correction. IR spectra were recorded on a VECTOR 22 spectrophotometer with KBr discs in the region 4000–400 cm^{-1} . UV/Vis spectroscopy was performed on a Shimadzu UV-3100 spectrophotometer. X-ray crystallographic analysis of **N₂Se₂-NMe₂** and **P₃-Bz₃** (Figure 2 and the Supporting Information, Figure S2 and Tables S1–S3) was performed on a Bruker Smart Apex CCD diffractometer with monochromated $\text{MoK}\alpha$ radiation ($\lambda = 0.71073 \text{ \AA}$) at 293 K by using the ω – 2θ scan mode. The data were corrected for Lorentz and polarization effects. The structures were solved by using direct methods and refined on F^2 by using the full-matrix least-squares technique on the SHELXTL-2000 program package.^[40] The redox data were obtained on a Zahner Electrochemical Workstation. The data were measured by using a platinum working electrode, a platinum-wire counter electrode, and a Ag/AgCl reference electrode with Fc/Fc^+ as an internal standard. The measurements were performed in CH_2Cl_2 with a 0.1 M Bu_4NPF_6 supporting electrolyte. All of the experiments were performed under an argon atmosphere. CCDC-905915 (**P₃-Bz₃**) and CCDC-639522 (**N₂Se₂-NMe₂**) contain the supplementary crystallographic data for this paper. These data can be obtained free of charge from The Cambridge Crystallographic Data Centre via www.ccdc.cam.ac.uk/data_request/cif

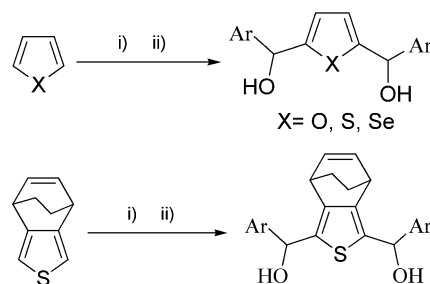
Optical spectroscopy: Electronic-absorption spectra were measured on Hitachi U-3410 and Cary 5000 UV/Vis/NIR spectrophotometers. Magnetic circular dichroism (MCD) spectra were recorded on a Jasco J-725 spectrodichromometer with a Jasco electromagnet that produced a magnetic field of up to 1.09 T. CHCl_3 that was stabilized by 0.5% EtOH (Nacalai Tesque) was used as the solvent for most of the MCD measurements. CDCl_3 was used when measurements at $\lambda > 1000 \text{ nm}$ were required. Trace amounts of triethylamine were added to solutions of **N₂Te₂**, **S₂N₂-F**, **P₁**, **P₃**, **P₁-Bz₃**, and **P₃-Bz₃** to prevent protonation. Steady-state fluorescence measurements were performed on a Spectronics Instrument 8100 spectrofluorometer. CHCl_3 and TFA, which were employed for the fluorescence measurements, were of UV spectroscopic grade. For all of the measurements, the temperature was kept constant at $298(\pm 1) \text{ K}$. All of the absorption measurements were performed in 10 mm cuvettes. Molar absorption coefficients were determined from $N = 4$ independent solutions and only very dilute stock solutions ($1\text{--}10 \mu\text{M}$) were used to avoid aggregation or solubility problems. The uncertainty of the measurements was $\pm 10\%$. Fluorescence studies were performed in 10 mm cuvettes (90°

standard geometry, no polarizers, 600 nm cut-off filter in the emission channel) with optically diluted solutions with an absorbance of between 0.05 and 0.1 at the maximum of the B band. Depending on the porphyrin, a wavelength of either 525 or 535 nm was used for excitation (B band). For all of the species studied, the fluorescence-excitation spectra matched their absorption spectra. The fluorescence quantum yields (Φ_f) were determined relative to **TPTPhenPH₂²⁺** ($\Phi_f = 8.0 \times 10^{-3}$).^[16] The fluorescence spectra presented herein were spectrally corrected.^[41] The uncertainty of the measurements for Φ_f was determined to be $\geq \pm 10\%$. Fluorescence lifetimes (τ_f) were determined by a unique customized laser-impulse fluorometer with picosecond time resolution.^[42] The fluorescence was collected at right angles (monochromator with spectroscopic bandwidths of 16 nm). Whilst realizing typical instrument response functions of $\text{fwhm} \approx 30 \text{ ps}$, the time division was $4.8 \text{ ps channel}^{-1}$ and the experimental accuracy was $\pm 3 \text{ ps}$, respectively. The laser beam was attenuated by using a double-prism attenuator (LTB) and typical excitation energies were in the nanowatt to microwatt range (average laser power). The fluorescence-lifetime profiles were analyzed by a PC with the Global Unlimited V2.2 software package (Laboratory for Fluorescence Dynamics, University of Illinois). The goodness of fit of the single decays, as judged by reduced chi-squared (χ_R^2) and the autocorrelation function ($C(j)$) of the residuals, was always below $\chi_R^2 < 1.2$.

Calculations Molecular structures were optimized and MO energies were obtained for **P**, free-base tetraphenylporphyrin (**TPP**), **TPhenP**, **TPTPhenP**, **2Phen₂N₄**, **N₂O₂**, **N₂O₂-OMe**, **N₂S₂**, **N₂S₂-OMe**, **N₂Se₂**, **N₂Se₂-OMe**, **P₁**, **P₁-Bz₃**, **P₃**, and **P₃-Bz₃**, and the X-ray structures of **N₂Se₂-NMe₂** and **P₃-Bz₃** (Figure 1, Figure 6, and the Supporting Information, Figures S4–S6) by using the B3LYP functional of the G03W software package^[43] with 6–31G(d) basis sets and for **N₂O₂**, **N₂S₂**, **N₂Se₂**, and **N₂Te₂** with the 3–21G** basis sets (see the Supporting Information, Figure S3). TD-DFT calculations were performed with the same basis sets (Figure 9, Figure 11, Figure 13, Table 1, and the Supporting Information, S1, S3–S6, and Tables S4 and S5) and the optimized structures were also used for ZINDO/s calculations (see the Supporting Information, Figures S7–S13 and Tables S6–S8).

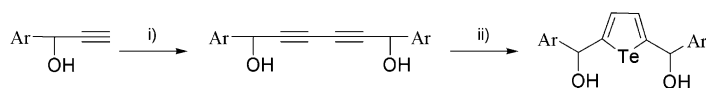
Synthesis: All of the experiments were performed under an inert argon atmosphere. Unless otherwise noted, all of the chemicals and solvents were of analytical reagent grade and used as received. Dry CH_2Cl_2 was freshly distilled over CaH_2 under a nitrogen atmosphere. Dry THF was distilled from sodium/benzophenone under a nitrogen atmosphere. Column chromatography and TLC were performed on C-200 (Wakogel) and Kieselgel 60 F254 (Merck), respectively. *para*-Hexadecyloxybenzaldehyde^[44] and phenanthro[9,10-*c*]pyrrole^[45] were prepared according to literature procedures.

General procedure for preparing diols: Dry and freshly distilled *n*-hexane (52 mL) was added to a three-necked, round-bottomed flask (250 mL) that was flushed with argon gas for 10 min. *N,N,N',N'*-Tetramethylethylenediamine (TMEDA, 4.8 mL, 32 mmol) and *n*-BuLi (20 mL, 1.6 M in *n*-hexane, 32 mmol) were added and the solution was stirred under an argon atmosphere for 10 min. Then, redistilled furan, thiophene, selenophene, or 4,7-dihydro-4,7-ethanoisothianaphthene (BCOD-fused thiophene; 16 mmol) was added and the solution was gently heated at reflux for 1 h (Schemes 1 and 2). The reaction mixture was cooled to 0°C



Scheme 1. Synthesis of the diols: i) TMEDA, *n*BuLi, dry *n*-C₆H₁₄; ii) ArCHO, dry THF.

in an ice bath and a solution of the aromatic aldehyde (33 mmol) in dry THF (32 mL) was added slowly. Next, the reaction mixture was allowed to warm to RT and was stirred for 15 min. The reaction was quenched by adding an ice-cold aqueous solution of NH_4Cl (48 mL, about 1 M). The organic layer was washed with water, brine, and dried with anhydrous Na_2SO_4 . The solvent was removed on a rotary evaporator under reduced pressure to afford the crude compounds, which were purified by column chromatography on silica gel to obtain the target compounds as white solids (Scheme 2).



Scheme 2. Synthesis of the tellurophene diols: i) CuCl/TMEDA in acetone; ii) NaHTe , CH_3OH , AgOAc , RT, 24 h.

2,5-Bis(phenylhydroxymethyl)furan: 2.01 g, 45%; ^1H NMR (500 MHz, CDCl_3): δ = 7.38–7.36 (m, 10H), 6.00–5.98 (m, 2H), 5.82 (s, 2H), 4.12 ppm (s, 2H).

2,5-Bis[(4-hexadecyloxyphenyl)hydroxymethyl]furan: 5.0 g, 41%; ^1H NMR (500 MHz, CDCl_3): δ = 7.66–7.64 (m, 4H), 7.23–7.20 (m, 4H), 6.03–5.99 (m, 2H), 5.74 (s, 2H), 3.86 (m, 4H), 1.79–1.77 (m, 4H), 1.30–1.26 (m, 52H), 0.91 ppm (t, 6H).

2,5-Bis(phenylhydroxymethyl)thiophene: 2.66 g, 56%; ^1H NMR (500 MHz, CDCl_3): δ = 7.44–7.45 (m, 4H), 7.34–7.40 (m, 4H), 7.31–7.33 (m, 2H), 6.72 (s, 2H), 5.97 (s, 2H), 2.46 ppm (brs, 2H); ^{13}C NMR (125 MHz, CD_3OD): 127.7, 127.5, 126.2, 124.3, 81.0, 77.5, 77.2, 77.0 ppm.

2,5-Bis[(4-hexadecyloxyphenyl)hydroxymethyl]thiophene: 6.8 g, 55%; ^1H NMR (500 MHz, CDCl_3): δ = 7.34 (d, 4H), 6.89 (d, 4H), 6.71 (s, 2H), 5.95–5.93 (m, 2H), 3.96 (t, 4H), 2.32–2.30 (m, 2H), 1.81–1.78 (m, 4H), 1.46–1.43 (m, 4H), 1.31–1.27 (m, 48H), 0.91 ppm (t, 6H).

2,5-Bis[(4-fluorophenyl)hydroxymethyl]thiophene: 3.56 g, 67%; ^1H NMR (500 MHz, CDCl_3): δ = 7.41–7.43 (m, 4H), 7.05–7.08 (m, 4H), 6.73 (s, 2H), 5.98 (s, 2H), 2.44 ppm (brs, 2H); ^{13}C NMR (125 MHz, CD_3OD): 162.8, 148.2, 139.6, 128.2, 127.4, 123.2, 114.2, 114.1, 114.0, 70.7 ppm.

2,5-Bis[(4-fluorophenyl)hydroxymethyl]4,7-dihydro-4,7-ethanoisothianaphthene: 1.12 g, 34%; ^1H NMR (500 MHz, CDCl_3): δ = 7.39–7.36 (m, 4H), 7.05–6.99 (m, 4H), 6.43–6.39 (m, 2H), 6.02 (d, J = 8.8 Hz, 2H), 3.80–3.77 (m, 2H), 2.23–2.21 (m, 2H), 1.55–1.42 ppm (m, 4H).

2,5-Bis(phenylhydroxymethyl)selenophene: 2.69 g, 49%; ^1H NMR (500 MHz, CDCl_3): δ = 7.49–7.26 (m, 10H), 6.88 (s, 2H), 5.97 (s, 2H), 2.42 ppm (brs, 2H).

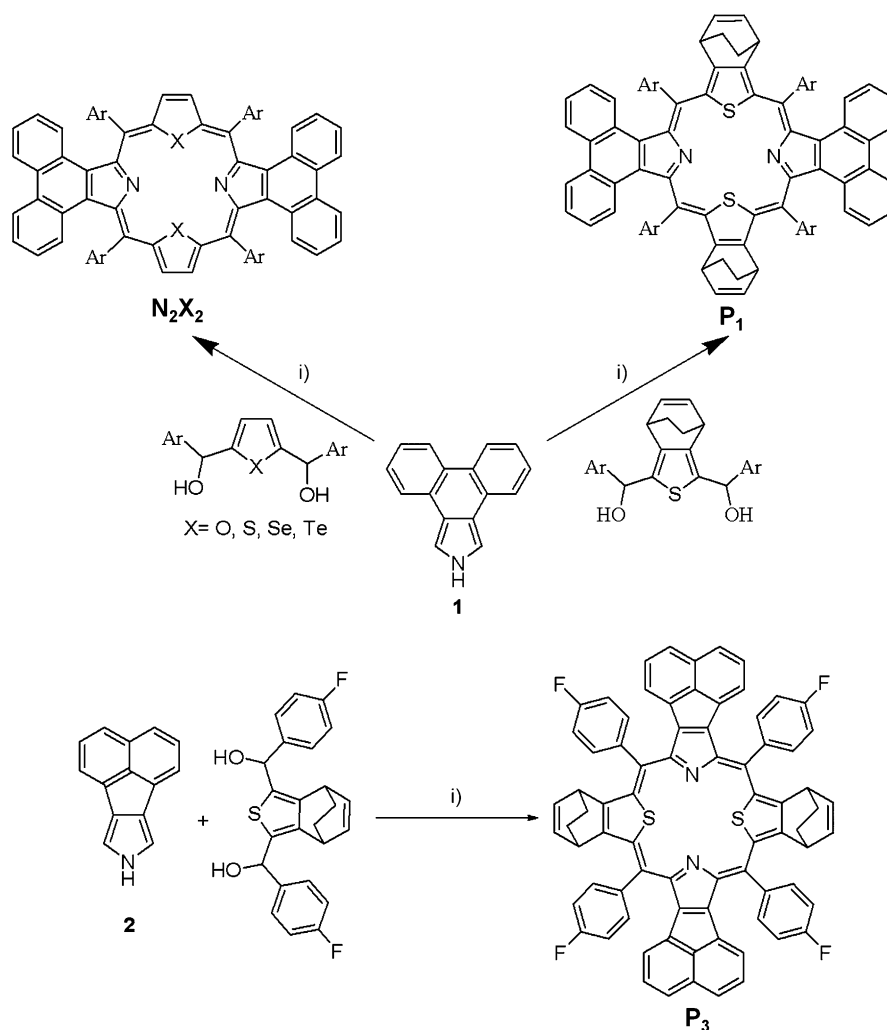
2,5-Bis[(4-hexadecyloxyphenyl)hydroxymethyl]selenophene: 6.33 g, 48%; ^1H NMR (500 MHz, CDCl_3):

δ = 7.35–7.33 (m, 4H), 6.89–6.88 (m, 4H), 6.80 (s, 2H), 5.94 (s, 2H), 3.97–3.94 (m, 4H), 2.31 (brs, 2H), 1.81–1.76 (m, 4H), 1.46–1.43 (m, 4H), 1.27 (s, 52H), 0.91–0.88 ppm (m, 6H).

2,5-Bis[(4-*N,N*-dimethylphenyl)hydroxymethyl]selenophene: 6.05 g, 88%; ^1H NMR (500 MHz, CDCl_3): δ = 7.36–7.35 (m, 4H), 7.01–6.95 (m, 4H), 6.80 (s, 2H), 5.90 (s, 2H), 2.40 (s, 12H), 2.33 ppm (brs, 2H).

2,5-Bis(phenylhydroxymethyl)tellurophene: 2,5-Bis(phenylhydroxymethyl)tellurophene was synthesized according to a literature procedure^[46] from NaHTe and 1,6-diphenylhexa-2,4-diyne-1,6-diol.^[47] The product was recrystallized from *n*-hexane/ CHCl_3 .

General procedure for the preparation of N_2Y_2 and $\text{BCOD-N}_2\text{S}_2$: The appropriate diol (1 mmol) was added to a stirring solution of phenanthropyrrole (217 mg, 1 mmol) in freshly dried and deoxygenated CH_2Cl_2 (100 mL) and the resulting solution was purged with argon for 10 min (Scheme 3). $\text{BF}_3\cdot\text{Et}_2\text{O}$ (40 μL , 0.32 mmol) was added and the reaction mixture was stirred for 3 h at -50°C in the dark and then warmed to RT and stirred for 24 h. After that, 2,3-dichloro-5,6-dicyano-1,4-benzoquinone (DDQ; 227 mg, 1 mmol) was added and the solution was stirred for an additional 12 h; then, the solvents were removed under reduced pressure by rotary evaporation. The crude product was purified by column chromatography on silica gel and recrystallized from $\text{CH}_2\text{Cl}_2/\text{CH}_3\text{OH}$. ^1H NMR spectroscopy and MS (MALDI-TOF) are provided in the Supporting Information, Figures S15–S35.



Scheme 3. Synthesis of the core-modified porphyrins: i) $\text{BF}_3\cdot\text{Et}_2\text{O}$, CH_2Cl_2 , -50°C , 3 h, then warm to RT, 24 h, then DDQ, 12 h.

5,10,15,20-Tetraphenyldiphenanthro[9,10-*b*:9,10-*f*]-21,23-dioxaporphyrin (N_2O_2): N_2O_2 was prepared as described above from 2,5-bis(phenylhydroxymethyl)furan (280 mg, 1 mmol), phenanthro[9,10-*c*]pyrrole (217 mg, 1 mmol), $BF_3 \cdot Et_2O$ (40 μ L, 0.32 mmol), and DDQ (227 mg, 1 mmol). Column chromatography on silica gel ($CHCl_3$, EtOAc/petroleum ether 50%), then $CHCl_3/CH_3OH$ 50%), followed by recrystallization from $CHCl_3/MeOH$, afforded dark-green crystals (91 mg, 32%). M.p. > 250 °C; 1H NMR (500 MHz, $[D_6]DMSO$): δ = 8.78 (s, 2H), 8.66–8.64 (m, 4H), 8.58–8.56 (m, 2H), 8.33–8.31 (m, 4H), 8.19 (s, 2H), 7.94–7.93 (m, 2H), 7.87–7.86 (m, 4H), 7.79–7.77 (m, 2H), 7.73–7.71 (m, 4H), 7.62–7.61 (m, 2H), 7.44–7.42 (m, 4H), 7.33–7.31 (m, 4H), 7.10–7.08 (m, 2H), 7.03–7.01 ppm (m, 2H); UV/Vis ($CHCl_3$): λ_{max} (ϵ) = 496 (75 100), 576 (12 700), 620 (8 170), 850 nm (4 670 $mol^{-1} dm^3 cm^{-1}$); MS (MALDI-TOF): m/z calcd for $C_{68}H_{41}N_2O_2$: 917.057 $[M+H]^+$; found: 917.366; elemental analysis calcd (%) for $C_{68}H_{40}N_2O_2$: C 89.06, H 4.40, N 3.05; found: C 89.02, H 4.39, N 2.99.

5,10,15,20-Tetra-4-methoxyphenyldiphenanthro[9,10-*b*:9,10-*f*]-21,23-dioxaporphyrin (N_2O_2-OMe): N_2O_2-OMe was prepared as described above from 2,5-bis(4-methoxyphenylhydroxymethyl)furan (340 mg, 1 mmol), phenanthro[9,10-*c*]pyrrole (217 mg, 1 mmol), $BF_3 \cdot Et_2O$ (40 μ L, 0.32 mmol), and DDQ (227 mg, 1 mmol). Column chromatography on silica gel ($CHCl_3$, EtOAc/petroleum ether 50%), then triethylamine (TEA)/ $CHCl_3$ 5%), followed by recrystallization from $CHCl_3/MeOH$, afforded dark-green crystals (91 mg, 32%). M.p. > 250 °C; 1H NMR (500 MHz, $[D_6]DMSO$): δ = 8.44–8.42 (m, 4H), 8.32–8.30 (m, 8H), 8.13–8.11 (m, 4H), 8.01–7.99 (m, 4H), 7.29–7.27 (m, 4H), 7.20–7.18 (m, 8H), 7.02–7.00 (m, 4H), 3.97–3.93 ppm (m, 12H); UV/Vis ($CHCl_3$): λ_{max} (ϵ) = 508 (118 100), 582 (25 700), 877 nm (9 410 $mol^{-1} dm^3 cm^{-1}$); MS (MALDI-TOF): m/z calcd for $C_{72}H_{48}N_2O_6$: 1036.35 $[M]^+$; found: 1036.55; elemental analysis calcd (%) for $C_{72}H_{48}N_2O_6$: C 83.38, H 4.66, N 2.70; found: C 83.31, H 4.76, N 2.70.

5,10,15,20-Tetra-4-hexadecyloxyphenyldiphenanthro[9,10-*b*:9,10-*f*]-21,23-dioxaporphyrin ($N_2O_2-OC_{16}H_{33}$): $N_2O_2-OC_{16}H_{33}$ was prepared as described above from 2,5-bis(4-hexadecyloxyphenylhydroxymethyl)furan (761 mg, 1 mmol), phenanthro[9,10-*c*]pyrrole (217 mg, 1 mmol), $BF_3 \cdot Et_2O$ (40 μ L, 0.32 mmol), and DDQ (227 mg, 1 mmol). Column chromatography on silica gel ($CHCl_3$, EtOAc/petroleum ether 50%), then $CHCl_3/CH_3OH$ 50%) afforded dark-green crystals (158 mg, 16%). M.p. 142 °C; 1H NMR (500 MHz, $CDCl_3$): δ = 8.47–8.44 (m, 4H), 8.32–8.25 (m, 8H), 8.16–8.14 (m, 4H), 8.04–8.02 (m, 4H), 7.27–7.30 (m, 4H), 7.12–7.20 (m, 8H), 7.02–7.05 (m, 4H), 4.09–4.12 (t, 8H), 1.90–1.88 (m, 8H), 1.56–1.55 (m, 8H), 1.35–1.30 (m, 96H), 0.93 ppm (t, 12H); UV/Vis ($CHCl_3$): λ_{max} (ϵ) = 516 (45 600), 630 (6 790), 877 nm (3 610 $mol^{-1} dm^3 cm^{-1}$); MS (MALDI-TOF): m/z calcd for $C_{132}H_{168}N_2O_6$: 1877.29; found: 1877.39; elemental analysis calcd (%) for $C_{132}H_{168}N_2O_6$: C 84.39, H 9.01, N 1.49; found: C 84.50, H 9.13, N 1.38.

5,10,15,20-Tetra-4-fluorophenyldiphenanthro[9,10-*b*:9,10-*f*]-21,23-dioxaporphyrin (N_2O_2-F): N_2O_2-F was prepared as described above from 2,5-bis(4-fluorophenylhydroxymethyl)furan (316 mg, 1 mmol), phenanthro[9,10-*c*]pyrrole (217 mg, 1 mmol), $BF_3 \cdot Et_2O$ (40 μ L, 0.32 mmol), and DDQ (227 mg, 1 mmol). Column chromatography on silica gel ($CHCl_3$, EtOAc/petroleum ether, then $CHCl_3/CH_3OH$ 50%), followed by recrystallization from $CHCl_3/MeOH$, afforded dark-green crystals (78.6 mg, 16%). M.p. > 250 °C; 1H NMR (500 MHz, $[D_6]DMSO$): δ = 8.75 (s, 4H), 8.64–8.63 (m, 8H), 8.27 (s, 4H), 7.85–7.84 (m, 4H), 7.67–7.64 (m, 8H), 7.44 (s, 4H), 7.13–7.10 ppm (m, 4H); UV/Vis ($CHCl_3$): λ_{max} (ϵ) = 497 (49 400), 577 (10 600), 622 (6 740), 851 nm (2 800 $mol^{-1} dm^3 cm^{-1}$); MS (MALDI-TOF): m/z calcd for $C_{68}H_{37}F_4N_2O_2$: 989.279 $[M+H]^+$; found: 989.347; elemental analysis calcd (%) for $C_{68}H_{36}F_4N_2$: C 82.58, H 3.67, N 2.83; found: C 82.35, H 3.65, N 2.97.

5,10,15,20-Tetra-4-chlorophenyldiphenanthro[9,10-*b*:9,10-*f*]-21,23-dioxaporphyrin (N_2O_2-Cl): N_2O_2-Cl was prepared as described above from 2,5-bis(4-chlorophenylhydroxymethyl)furan (349 mg, 1 mmol), phenanthro[9,10-*c*]pyrrole (217 mg, 1 mmol), $BF_3 \cdot Et_2O$ (40 μ L, 0.32 mmol), and DDQ (227 mg, 1 mmol). Column chromatography on silica gel ($CHCl_3$, EtOAc/petroleum ether, then $CHCl_3/CH_3OH$ 50%), followed by recrystallization from $CHCl_3/MeOH$, afforded dark-green crystals (55 mg, 10%). M.p. > 250 °C; 1H NMR (500 MHz, $[D_6]DMSO$): δ = 8.79 (s, 4H),

8.69–8.67 (m, 8H), 8.29 (s, 4H), 7.86–7.84 (m, 8H), 7.48–7.45 (m, 4H), 7.15–7.12 ppm (m, 8H); UV/Vis ($CHCl_3$): λ_{max} (ϵ) = 491 (32 900), 627 (4 630), 852 nm (1 490 $mol^{-1} dm^3 cm^{-1}$); MS (MALDI-TOF): m/z calcd for $C_{68}H_{36}Cl_4N_2O_2$: 1055.845; found: 1055.209; elemental analysis calcd (%) for $C_{68}H_{36}Cl_4N_2O_2$: C 77.43, H 3.44, N 2.66; found: C 77.26, H 3.65, N 2.76.

5,10,15,20-Tetra-4-bromophenyldiphenanthro[9,10-*b*:9,10-*f*]-21,23-dioxaporphyrin (N_2O_2-Br): N_2O_2-Br was prepared as described above from 2,5-bis(4-bromophenylhydroxymethyl)furan (438 mg, 1 mmol), phenanthro[9,10-*c*]pyrrole (217 mg, 1 mmol), $BF_3 \cdot Et_2O$ (40 μ L, 0.32 mmol), and DDQ (227 mg, 1 mmol). Column chromatography on silica gel ($CHCl_3$, EtOAc/petroleum ether 50%), then $CHCl_3/CH_3OH$ 50%), followed by recrystallization from $CHCl_3/MeOH$, afforded dark-green crystals (121 mg, 19%). M.p. > 250 °C; 1H NMR (500 MHz, $[D_6]DMSO$): δ = 8.79–8.77 (m, 4H), 8.68–8.66 (m, 4H), 8.57–8.54 (m, 8H), 8.01–7.99 (m, 8H), 7.86–7.84 (m, 4H), 7.48–7.45 (m, 4H), 7.15–7.12 ppm (m, 4H); UV/Vis ($CHCl_3$): λ_{max} (ϵ) = 488 (94 100), 580 (16 000), 631 (8 400), 854 nm (6 210 $mol^{-1} dm^3 cm^{-1}$); MS (MALDI-TOF): m/z calcd for $C_{68}H_{36}Br_4N_2O_2$: 1233.649 $[M+H]^+$; found: 1233.037; elemental analysis calcd (%) for $C_{68}H_{36}Br_4N_2O_2$: C 66.26, H 2.94, N 2.27; found: C 66.20, H 2.95, N 2.17.

5,10,15,20-Tetra-4-iodophenyldiphenanthro[9,10-*b*:9,10-*f*]-21,23-dioxaporphyrin (N_2O_2-I): N_2O_2-I was prepared as described above from 2,5-bis(4-iodophenylhydroxymethyl)furan (532 mg, 1 mmol), phenanthro[9,10-*c*]pyrrole (217 mg, 1 mmol), $BF_3 \cdot Et_2O$ (40 μ L, 0.32 mmol), and DDQ (227 mg, 1 mmol). Column chromatography on silica gel ($CHCl_3$, EtOAc/petroleum ether 50%), then $CHCl_3/CH_3OH$ 50%), followed by recrystallization from $CHCl_3/MeOH$, afforded dark-green crystals (119 mg, 17%). M.p. > 250 °C; 1H NMR (500 MHz, $[D_6]DMSO$): δ = 8.49–8.47 (m, 4H), 8.15–8.13 (m, 4H), 8.08–8.05 (m, 8H), 8.00–7.99 (m, 8H), 7.90–7.89 (m, 4H), 7.37–7.34 (m, 4H), 7.07–7.04 ppm (m, 4H); UV/Vis ($CHCl_3$): λ_{max} (ϵ) = 499 (98 600), 582 (17 400), 631 (8 510), 856 nm (5 170 $mol^{-1} dm^3 cm^{-1}$); MS (MALDI-TOF): m/z calcd for $C_{68}H_{37}I_4N_2O_2$: 1420.903 $[M+H]^+$; found: 1420.968; elemental analysis calcd (%) for $C_{68}H_{36}I_4N_2O_2$: C 57.49, H 2.55, N 1.97; found: C 57.49, H 2.69, N 1.94.

5,10,15,20-Tetraphenyldiphenanthro[9,10-*b*:9,10-*f*]-21,23-dithiaporphyrin (N_2S_2): Dark-green crystals (72 mg, 15%); M.p. > 250 °C; 1H NMR (500 MHz, $CDCl_3$): δ = 8.86 (s, 4H), 8.66 (d, J = 8.3 Hz, 4H), 8.41 (d, J = 7.2 Hz, 8H), 8.02 (d, J = 8.3 Hz, 4H), 7.72–7.69 (m, 8H), 7.63–7.61 (m, 4H), 7.41–7.37 (m, 4H), 6.99–6.96 ppm (m, 4H); UV/Vis (CH_2Cl_2): λ_{max} (ϵ) = 505 (124 000), 583 (25 000), 817 nm (4 500 $mol^{-1} dm^3 cm^{-1}$); MS (MALDI TOF): m/z calcd for $C_{68}H_{40}N_2S_2$: 949.2711; found: 949.590; HRMS (FAB): m/z calcd for $C_{68}H_{40}N_2S_2$: 949.2711; found: 949.2715.

5,10,15,20-Tetra-4-hexadecyloxyphenyldiphenanthro[9,10-*b*:9,10-*f*]-21,23-dithiaporphyrin ($N_2S_2-OC_{16}H_{33}$): Dark-green crystals (171 mg, 18%); M.p. 145 °C; 1H NMR (500 MHz, $CDCl_3$): δ = 8.86 (s, 4H), 8.50 (d, J = 8.5 Hz, 4H), 8.43 (d, J = 8.0 Hz, 8H), 8.07 (d, J = 8.5 Hz, 4H), 7.35–7.33 (m, 4H), 7.21–7.19 (m, 8H), 6.98–6.96 (m, 4H), 4.08 (t, J = 6.0 Hz, 8H), 1.88–1.86 (m, 8H), 1.56–1.53 (m, 8H), 1.32–1.28 (m, 96H), 0.91 ppm (t, J = 8.5 Hz, 12H); UV/Vis (CH_2Cl_2): λ_{max} (ϵ) = 410 (27 177), 510 (141 362), 588 nm (27 275 $mol^{-1} dm^3 cm^{-1}$); MS (MALDI TOF): m/z calcd for $C_{132}H_{168}N_2O_4S_2$: 1909.24; found: 1909.60; elemental analysis calcd (%) for $C_{132}H_{168}N_2O_4S_2$: C 82.97, H 8.86, N 1.47; found: C 82.87, H 8.89, N 1.61.

5,10,15,20-Tetra-4-fluorophenyldiphenanthro[9,10-*b*:9,10-*f*]-21,23-dithiaporphyrin (N_2S_2-F): Dark-green crystals (67 mg, 13%); M.p. > 250 °C; 1H NMR (500 MHz, $[D_6]DMSO$): δ = 8.94 (s, 4H), 8.79 (d, J = 8.3 Hz, 4H), 8.56–8.53 (m, 8H), 8.07 (d, J = 8.2 Hz, 4H), 7.65–7.61 (m, 8H), 7.54–7.51 (m, 4H), 7.17–7.15 ppm (m, 4H); UV/Vis (CH_2Cl_2): λ_{max} (ϵ) = 506 (123 000), 586 (26 000), 817 (4 420) 500 (123 000), 575 (26 000), 813 nm (4 420 $mol^{-1} dm^3 cm^{-1}$); MS (MALDI TOF): m/z calcd for $C_{68}H_{36}F_4N_2S_2$: 1021.150; found: 1022.590; HRMS (FAB): m/z calcd for $C_{68}H_{36}F_4N_2S_2$: 1021.2334 $[M+H]^+$; found: 1021.2337.

5,10,15,20-Tetraphenyldiphenanthro[9,10-*b*:9,10-*f*]-21,23-diselenaporphyrin (N_2Se_2): N_2Se_2 was prepared as described above from 2,5-bis(phenylhydroxymethyl)selenophene (343 mg, 1 mmol), phenanthro[9,10-*c*]pyrrole (217 mg, 1 mmol), $BF_3 \cdot Et_2O$ (80 μ L, 0.64 mmol), and DDQ (227 mg, 1 mmol). Column chromatography on silica gel ($CHCl_3$ then EtOH/ $CHCl_3$ 2%), followed by recrystallization from $CHCl_3/MeOH$, afforded

dark-green crystals (103 mg, 19.7%). M.p. > 250 °C; ^1H NMR (500 MHz, CDCl_3): δ = 8.71 (s, 4H), 8.65–8.63 (m, 4H), 8.50 (brs, 8H), 8.28–8.25 (m, 4H), 7.73–7.70 (m, 8H), 7.62–7.60 (m, 4H), 7.45 (m, 4H), 7.10 ppm (brs, 4H); UV/Vis (CHCl_3): λ_{max} (ϵ) = 505 (227300), 580 (54200), 810 nm ($11300 \text{ mol}^{-1} \text{ dm}^3 \text{ cm}^{-1}$); MS (MALDI-TOF): m/z calcd for $\text{C}_{68}\text{H}_{40}\text{N}_2\text{Se}_2$: 1044.152; found: 1044.477; elemental analysis calcd (%) for $\text{C}_{68}\text{H}_{40}\text{N}_2\text{Se}_2$: C 78.31, H 3.87, N 2.69; found: C 78.25, H 3.71, N 2.65.

5,10,15,20-Tetra-4-hexadecyloxyphenyldiphenanthro[9,10-*b*:9,10-*I*]-21,23-diselenaporphyrin ($\text{N}_2\text{Se}_2\text{-OC}_{16}\text{H}_{33}$): $\text{N}_2\text{Se}_2\text{-OC}_{16}\text{H}_{33}$ was prepared as described above from 2,5-bis(4-hexadecyloxyphenylhydroxymethyl)selenophene (824 mg, 1 mmol), phenanthro[9,10-*c*]pyrrole (217 mg, 1 mmol), $\text{BF}_3\cdot\text{Et}_2\text{O}$ (80 μL , 0.64 mmol), and DDQ (227 mg, 1 mmol). Column chromatography on silica gel (CHCl_3 then $\text{EtOH}/\text{CHCl}_3$ 2%), followed by recrystallization from $\text{CHCl}_3/\text{MeOH}$, afforded dark-green crystals (414 mg, 41%). M.p. 151 °C; ^1H NMR (500 MHz, CDCl_3): δ = 8.68 (s, 4H), 8.63 (d, 4H), 8.43–8.41 (m, 8H), 7.30–7.27 (m, 4H), 7.44–7.41 (m, 4H), 7.25–7.21 (m, 8H), 7.14–7.11 (m, 4H), 4.13 ppm (t, 8H), 1.99–1.94 (m, 8H), 1.59–1.46 (m, 8H), 1.35–1.27 (m, 96H), 0.93 (t, 12H); UV/Vis (CHCl_3): λ_{max} (ϵ) = 530 (91500), 606 (25600), 849 nm ($6850 \text{ mol}^{-1} \text{ dm}^3 \text{ cm}^{-1}$); MS (MALDI-TOF): m/z calcd for $\text{C}_{132}\text{H}_{169}\text{N}_2\text{O}_4\text{Se}_2$: 2006.14 [$M+\text{H}$] $^+$; found: 2006.88; elemental analysis calcd (%) for $\text{C}_{132}\text{H}_{168}\text{N}_2\text{O}_4\text{Se}_2$: C 79.09, H 8.45, N 1.40; found: C 79.09, H 8.43, N 1.49.

5,10,15,20-Tetra-4-methoxyphenyldiphenanthro[9,10-*b*:9,10-*I*]-21,23-diselenaporphyrin ($\text{N}_2\text{Se}_2\text{-OMe}$): $\text{N}_2\text{Se}_2\text{-OMe}$ was prepared as described above from 2,5-bis(4-hexadecyloxyphenylhydroxymethyl)selenophene (824 mg, 1 mmol), phenanthro[9,10-*c*]pyrrole (217 mg, 1 mmol), $\text{BF}_3\cdot\text{Et}_2\text{O}$ (80 μL , 0.64 mmol), and DDQ (227 mg, 1 mmol). Column chromatography on silica gel (CHCl_3 then $\text{EtOH}/\text{CHCl}_3$ 2%), followed by recrystallization from $\text{CHCl}_3/\text{MeOH}$, afforded dark-green crystals (255 mg, 44%). M.p. > 250 °C; ^1H NMR (500 MHz, CDCl_3): δ = 8.65–8.63 (m, 8H), 8.44–8.42 (m, 8H), 8.28 (d, J = 8.5 Hz, 4H), 7.45–7.42 (m, 4H), 7.26–7.22 (m, 8H), 7.15–7.12 (m, 4H), 3.99 ppm (s, 12H); UV/Vis (CHCl_3): λ_{max} (ϵ) = 526 (102800), 605 (26900), 844 nm ($7500 \text{ mol}^{-1} \text{ dm}^3 \text{ cm}^{-1}$); MS (MALDI-TOF): m/z calcd for $\text{C}_{72}\text{H}_{48}\text{N}_2\text{O}_4\text{Se}_2$: 1164.194; found: 1164.891; elemental analysis calcd (%) for $\text{C}_{72}\text{H}_{48}\text{N}_2\text{O}_4\text{Se}_2$: C 74.35, H 4.16, N 2.41; found: C 74.23, H 4.13, N 2.25.

5,10,15,20-Tetra-4-dimethylaminophenyldiphenanthro[9,10-*b*:9,10-*I*]-21,23-diselenaporphyrin ($\text{N}_2\text{Se}_2\text{-NMe}_2$): $\text{N}_2\text{Se}_2\text{-NMe}_2$ was prepared as described above from 2,5-bis(4-hexadecyloxyphenylhydroxymethyl)selenophene (429 mg, 1 mmol), phenanthro[9,10-*c*]pyrrole (217 mg, 1 mmol), $\text{BF}_3\cdot\text{Et}_2\text{O}$ (80 μL , 0.64 mmol), and DDQ (227 mg, 1 mmol). Column chromatography on silica gel (CHCl_3 , $\text{EtOH}/\text{CHCl}_3$ 2%, then TEA/CHCl_3 5%), followed by recrystallization from $\text{CHCl}_3/\text{MeOH}$, afforded dark-green crystals (457 mg, 75%). M.p. > 250 °C; ^1H NMR (500 MHz, $\text{CH}_3\text{CH}_2\text{OD}/\text{CDCl}_3$, 1:1): δ = 8.51–8.48 (m, 4H), 8.49–8.41 (m, 8H), 8.14–8.12 (m, 4H), 7.38–7.36 (m, 4H), 7.28–7.25 (m, 4H), 7.11–7.08 (m, 4H), 6.97–6.96 (m, 8H), 3.27 ppm (s, 24H); UV/Vis (CHCl_3): λ_{max} (ϵ) = 444 (5867), 593 nm ($83841 \text{ mol}^{-1} \text{ dm}^3 \text{ cm}^{-1}$); MS (MALDI-TOF): m/z calcd for $\text{C}_{76}\text{H}_{60}\text{N}_6\text{Se}_2$: 1215.250; found: 1215.055; elemental analysis calcd (%) for $\text{C}_{76}\text{H}_{60}\text{N}_6\text{Se}_2$: C 75.11, H 4.98, N 6.92; found: C 74.99, H 4.96, N 6.78.

5,10,15,20-Tetra-4-phenyldiphenanthro[9,10-*b*:9,10-*I*]-21,23-ditelluroporphyrin (N_2Te_2): N_2Te_2 was prepared as described above from 2,5-bis(phenylhydroxymethyl)tellurophene (391 mg, 1 mmol), phenanthro[9,10-*c*]pyrrole (217 mg, 1 mmol), $\text{BF}_3\cdot\text{Et}_2\text{O}$ (80 μL , 0.64 mmol), and DDQ (227 mg, 1 mmol). Column chromatography on silica gel (CHCl_3), followed by recrystallization from $\text{CHCl}_3/\text{MeOH}$, afforded dark-green crystals (135 mg; 24%). M.p. > 250 °C; ^1H NMR (500 MHz, CDCl_3): δ = 8.71 (s, 4H), 8.63–8.65 (m, 4H), 8.51–8.49 (m, 8H), 8.26–8.27 (m, 4H), 7.72–7.70 (m, 8H), 7.62–7.59 (m, 4H), 7.45–7.43 (m, 4H), 7.12–7.09 ppm (m, 4H); UV/Vis (CHCl_3): λ_{max} (ϵ) = 528 (38864), 653 nm ($8612 \text{ mol}^{-1} \text{ dm}^3 \text{ cm}^{-1}$); MS (MALDI-TOF): m/z calcd for $\text{C}_{68}\text{H}_{40}\text{N}_2\text{Te}_2$: 1140.26; found: 1142.03; elemental analysis calcd (%) for $\text{C}_{68}\text{H}_{40}\text{N}_2\text{Te}_2$: C 71.63, H 3.54, N 2.46; found: C 71.51, H 3.61, N 2.61.

5,10,15,20-Tetra-4-fluorophenyldiphenanthro[9,10-*b*:9,10-*I*]-2 1 ,2 1 ,12 1 ,12 1 -tetrahydro-2 1 ,2 1 ,12 1 ,12 1 -diethano-21,23-dithiaporphyrin (P_4): Dark-green crystals (80 mg, 14%); M.p. > 300 °C; ^1H NMR (500 MHz, CDCl_3): δ = 9.09–9.07 (m, 4H), 8.55–8.53 (m, 4H), 8.33–8.31 (m, 4H), 7.85–7.83 (m, 4H), 7.32–7.30 (m, 8H), 7.45–7.42 (m, 2H), 7.36–7.33 (m, 4H), 7.08–7.06

(m, 2H), 6.99–6.97 (m, 4H), 3.68–3.65 (m, 4H), 1.49–1.45 ppm (m, 8H); UV/Vis (CH_2Cl_2): λ_{max} (ϵ) = 533 (152000), 607 (28000), 671 (16000), 861 nm ($11000 \text{ mol}^{-1} \text{ dm}^3 \text{ cm}^{-1}$); HRMS (FAB): m/z calcd for $\text{C}_{80}\text{H}_{49}\text{F}_4\text{N}_2\text{S}_2$: 1177.3273 [$M+\text{H}$] $^+$; found: 1177.3290.

5,10,15,20-Tetra-4-fluorophenyldiacenaphtho[1,2-*b*:1,2-*I*]-2 1 ,2 1 ,12 1 ,12 1 -tetrahydro-2 1 ,2 1 ,12 1 ,12 1 -diethano-21,23-dithiaporphyrin (P_3): Dark-green crystals (188 mg, 48%); M.p. > 300 °C; ^1H NMR (500 MHz, CDCl_3): δ = 8.61–8.43 (m, 8H), 7.80–7.64 (m, 12H), 7.28–7.26 (m, 4H), 6.71–6.69 (m, 2H), 6.37 (brs, 2H), 5.75 (t, J = 6.8 Hz, 4H), 3.75–3.71 (m, 4H), 1.54–1.24 ppm (m, 8H); UV/Vis (CH_2Cl_2): λ_{max} (ϵ) = 502 (106000), 582 (23100), 612 (14500), 714 (2740), 798 nm ($5000 \text{ mol}^{-1} \text{ dm}^3 \text{ cm}^{-1}$); HRMS (FAB): m/z calcd for $\text{C}_{76}\text{H}_{44}\text{F}_4\text{N}_2\text{S}_2$: 1125.2960 [$M+\text{H}$] $^+$; found: 1125.2961.

P_1 -Bz $_2$ and P_3 -Bz $_2$: Compounds P_1 -Bz $_2$ and P_3 -Bz $_2$ were obtained in quantitative yield by heating P_1 and P_3 in sample tubes under vacuum (2 mmHg) at 300 °C for 30 min.

5,10,15,20-Tetra-4-fluorophenyldiphenanthro[9,10-*b*:9,10-*I*]-21,23-dithiadibenzo[*b*,*I*]porphyrin (P_1 -Bz $_2$): ^1H NMR (500 MHz, CDCl_3): δ = 8.97–8.94 (m, 4H), 8.50 (d, J = 8.6 Hz, 4H), 8.09–8.06 (m, 4H), 7.72 (d, J = 7.8 Hz, 4H), 7.61–7.57 (m, 4H), 7.56–7.50 (m, 4H), 7.36–7.33 (m, 4H), 7.20–7.15 (m, 4H), 7.03–6.96 ppm (m, 8H); UV/Vis (CH_2Cl_2): λ_{max} (ϵ) = 543 (210000), 645 (23000), 712 (53000), 869 nm ($15000 \text{ mol}^{-1} \text{ dm}^3 \text{ cm}^{-1}$); HRMS (FAB): m/z calcd for $\text{C}_{76}\text{H}_{41}\text{F}_4\text{N}_2\text{S}_2$: 1121.2647 [$M+\text{H}$] $^+$; found: 1121.2660.

5,10,15,20-Tetra-4-fluorophenyldiacenaphtho[1,2-*b*:1,2-*I*]-21,23-dithiadibenzo[*b*,*I*]porphyrin (P_3 -Bz $_2$): ^1H NMR (500 MHz, CDCl_3): δ = 8.54–8.50 (m, 8H), 7.68–7.63 (m, 17H), 7.36–7.34 (m, 4H), 7.25–7.23 (m, 3H), 5.75 ppm (d, J = 7.1 Hz, 4H); UV/Vis (CH_2Cl_2): λ_{max} (ϵ) = 516 (135000), 708 (35800), 746 nm ($33600 \text{ mol}^{-1} \text{ dm}^3 \text{ cm}^{-1}$); HRMS (FAB): m/z calcd for $\text{C}_{72}\text{H}_{36}\text{F}_4\text{N}_2\text{S}_2$: 1069.2334 [$M+\text{H}$] $^+$; found: 1069.2335.

Acknowledgements

Financial support from the Major State Basic Research Development Program of China (Grant No. 2011CB808704), the National Natural Science Foundation of China (Nos. 20971066 and 21021062), Grants-in-Aid for Scientific Research on Innovative Areas (No. 20108007, “ π -Space”) and for Scientific Research B (No. 23350095) to N.K. by the Ministry of Education, Culture, Sports, Science, and Technology, Japan (MEXT), the Alexander-von-Humboldt Foundation, the European Commission’s Human Resources and Mobility Programme for a Marie Curie Intra-European Fellowship, and the Adolf-Martens Fonds is highly appreciated. We thank Dr. Atsuya Muranaka of the Institute of Physical and Chemical Research (Riken), Saitama, Japan for help with MCD measurements in the near-IR region.

- [1] a) S. Fox, R. W. Boyle, *Tetrahedron* **2006**, 62, 10039–10054; b) M. R. Detty, S. L. Gibson, S. J. Wagner, *J. Med. Chem.* **2004**, 47, 3897–3915; c) I. J. Macdonald, T. J. Dougherty, *J. Porphyrins Phthalocyanines* **2001**, 5, 105–129; d) R. Bonnett, *Chem. Soc. Rev.* **1995**, 24, 19–33; e) Z. Zhang, G. M. Ferrence, T. D. Lash, *Org. Lett.* **2009**, 11, 1249–1252.
- [2] a) T. Lu, P. Shao, I. Mathew, A. Sand, W. Sun, *J. Am. Chem. Soc.* **2008**, 130, 15782–15783; b) L. J. Jiao, B. H. Courtney, F. R. Fronczek, K. M. Smith, *Tetrahedron Lett.* **2006**, 47, 501–504; c) C. Comuzzi, S. Cogoi, M. Overhand, G. A. Van der Marel, H. S. Overkleeft, L. E. Xodo, *J. Med. Chem.* **2006**, 49, 196–204; d) M. Nath, M. Pink, J. M. Zaleski, *J. Am. Chem. Soc.* **2005**, 127, 478–479; e) M. Drobizhev, Y. Stepanenko, Y. Dzenis, A. Karotki, A. Rebane, P. N. Taylor, H. L. Anderson, *J. Phys. Chem. B* **2005**, 109, 7223–7236.
- [3] a) W. R. Dichtel, J. M. Serin, C. Edler, J. M. J. Fréchet, M. Matuszewski, L. Tan, T. Y. Ohulchanskyy, P. N. Prasad, *J. Am. Chem. Soc.* **2004**, 126, 5380–5381; b) R. N. S. van der Haas, R. L. P. de Jong, M. Noushazar, K. Erkelens, T. G. M. Smijs, Y. Liu, P. Gast, H. J. Schuitmaker, J. Lugtenburg, *Eur. J. Org. Chem.* **2004**, 4024–4038.

- [4] a) Y. Ikawa, M. Takeda, M. Suzuki, A. Osuka, H. Furuta, *Chem. Commun.* **2010**, 46, 5689–5691; b) F. Niedermair, S. M. Borisov, G. Zenkl, O. T. Hotmann, H. Weber, R. Saf, I. Klimant, *Inorg. Chem.* **2010**, 49, 9333–9342; c) C. Ikeda, N. Sakamoto, T. Nabeshima, *Org. Lett.* **2008**, 10, 4601–4604; d) D. Wu, A. B. Descalzo, F. Weik, F. Emmerling, Z. Shen, X.-Z. You, K. Rurack, *Angew. Chem.* **2008**, 120, 199–203; *Angew. Chem. Int. Ed.* **2008**, 47, 193–197; e) X.-J. Zhu, S.-T. Fu, W.-K. Wong, J.-P. Guo, W.-Y. Wong, *Angew. Chem.* **2006**, 118, 3222–3226; *Angew. Chem. Int. Ed.* **2006**, 45, 3150–3154.
- [5] a) D. Wu, Z. Shen, Z.-L. Xue, X.-Z. You, *Chin. J. Inorg. Chem.* **2007**, 23, 1–14; b) J. A. A. W. Elemans, R. Van Hameren, R. J. M. Nolte, A. E. Rowan, *Adv. Mater.* **2006**, 18, 1251–1266; c) C.-P. Hsieh, H.-P. Lu, C.-L. Chiu, C.-W. Lee, S.-H. Chuang, C.-L. Mai, W.-N. Yen, S.-J. Hsu, E. W.-G. Diau, C.-Y. Yeh, *J. Mater. Chem.* **2010**, 20, 1127–1134; d) S. Hayashi, M. Tanaka, H. Hayashi, S. Eu, T. Umeyama, Y. Matano, Y. Araki, H. Imahori, *J. Phys. Chem. C* **2008**, 112, 15576–15585.
- [6] a) T. V. Duncan, P. R. Frail, I. R. Miloradovic, M. J. Therien, *J. Phys. Chem. B* **2010**, 114, 14696–14702; b) S. Cho, J. M. Lim, S. Hiroto, P. Kim, H. Shinokubo, A. Osuka, D. Kim, *J. Am. Chem. Soc.* **2009**, 131, 6412–6420; c) M.-C. Yoon, R. Mira, Z. S. Yoon, K. S. Kim, J. M. Lim, T. K. Chandrashekar, D. Kim, *J. Phys. Chem. B* **2008**, 112, 6900–6905; d) M. Morone, L. Beverina, A. Abboto, F. Silvestri, E. Collini, C. Ferrante, R. Bozio, G. A. Pagani, *Org. Lett.* **2006**, 8, 2719–2722; e) M. Calvete, G. Y. Yang, M. Hanack, *Synth. Met.* **2004**, 141, 231–243.
- [7] a) D. Holten, D. F. Bocian, J. S. Lindsey, *Acc. Chem. Res.* **2002**, 35, 57–69; b) X. He, H. Liu, Y. Li, Y. Liu, F. Lu, Y. Li, D. Zhu, *Macromol. Chem. Phys.* **2005**, 206, 2199–2205; c) R. Iqbal, S. C. Moratti, A. B. Holmes, G. Yahiolglu, L. R. Milgrom, F. Cacialli, J. Morgado, R. H. Friend, *J. Mater. Sci.: Mater. Electron.* **2000**, 11, 97–103; d) R. W. Wagner, J. S. Lindsey, J. Seth, V. Palaniappan, D. F. Bocian, *J. Am. Chem. Soc.* **1996**, 118, 3996–3997.
- [8] a) H. Imahori, *J. Phys. Chem. B* **2004**, 108, 6130–6143; b) Z. Li, D. Wang, Y. Shi, P. Wang, X. Wang, *Mater. Chem. Phys.* **2005**, 90, 203–206.
- [9] a) T. L. Ma, K. Inoue, H. Noma, K. Yao, E. Abe, *J. Photochem. Photobiol. A* **2002**, 152, 207–212.
- [10] a) T. D. Lash, *J. Porphyrins Phthalocyanines* **2001**, 5, 267–288; b) T. D. Lash in *The Porphyrin Handbook*, Vol. 2 (Eds.: K. M. Kadish, K. M. Smith, R. Guilard), Academic Press, New York, **1999**, Chapter 10, pp. 125–199, and references therein; c) N. K. S. Davis, M. Pawlicki, H. L. Anderson, *Org. Lett.* **2008**, 10, 3945–3947; d) J. M. Manley, T. J. Roper, T. D. Lash, *J. Org. Chem.* **2005**, 70, 874–891; e) N. Ono, T. Yamamoto, N. Shimada, K. Kuroki, M. Wada, R. Utsunomiya, T. Yano, H. Uno, T. Murashima, *Heterocycles* **2003**, 61, 433–447.
- [11] a) I. A. Maretina, *Russ. J. Gen. Chem.* **2009**, 79, 1544–1581; b) H. L. Anderson, *Chem. Commun.* **1999**, 2323–2330; c) H. Zou, M. J. Therien, J. K. Blasie, *J. Phys. Chem. B* **2008**, 112, 1350–1357; d) M. U. Winters, J. Karnbratt, M. Eng, C. J. Wilson, H. L. Anderson, B. Albinsson, *J. Phys. Chem. C* **2007**, 111, 7192–7199; e) Z. Shen, H. Uno, Y. Shimizu, N. Ono, *Org. Biomol. Chem.* **2004**, 2, 3442–3447; f) S. M. Kuebler, R. G. Denning, H. L. Anderson, *J. Am. Chem. Soc.* **2000**, 122, 339–347.
- [12] P. N. Taylor, A. P. Wylie, J. Huuskonen, H. L. Anderson, *Angew. Chem.* **1998**, 110, 1033–1037; *Angew. Chem. Int. Ed.* **1998**, 37, 986–989.
- [13] a) R. Misra, T. K. Chandrashekar, *Acc. Chem. Res.* **2008**, 41, 265–279; b) J. L. Sessler, D. Seidel, *Angew. Chem.* **2003**, 115, 5292–5333; *Angew. Chem. Int. Ed.* **2003**, 42, 5134–5175; c) J. S. Reddy, V. G. Anand, *J. Am. Chem. Soc.* **2009**, 131, 15433–15439; d) Y. Kamimura, S. Shimizu, A. Osuka, *Chem. Eur. J.* **2007**, 13, 1620–1628; e) Y. Inokuma, T. Matsunari, N. Ono, H. Uno, A. Osuka, *Angew. Chem.* **2005**, 117, 1890–1894; *Angew. Chem. Int. Ed.* **2005**, 44, 1856–1860.
- [14] J. Mack, Y. Asano, N. Kobayashi, M. J. Stillman, *J. Am. Chem. Soc.* **2005**, 127, 17697–17711.
- [15] J. Mack, M. Bunya, Y. Shimizu, H. Uoyama, N. Komobuchi, T. Okujima, H. Uno, S. Ito, M. J. Stillman, N. Ono, N. Kobayashi, *Chem. Eur. J.* **2008**, 14, 5001–5020.
- [16] H.-J. Xu, J. Mack, A. B. Descalzo, Z. Shen, N. Kobayashi, X.-Z. You, K. Rurack, *Chem. Eur. J.* **2011**, 17, 8965–8983.
- [17] a) C. E. Stilts, M. I. Nelen, D. G. Hilmey, S. R. Davies, S. O. Gollnick, A. R. Oseroff, S. L. Gibson, R. Hilf, M. R. Detty, *J. Med. Chem.* **2000**, 43, 2403–2410; b) D. G. Hilmey, M. Abe, M. I. Nelen, C. E. Stilts, G. A. Baker, S. N. Baker, F. V. Bright, S. R. Davies, S. O. Gollnick, A. R. Oseroff, S. L. Gibson, R. Hilf, M. R. Detty, *J. Med. Chem.* **2002**, 45, 449–461; c) Y. You, S. L. Gibson, R. Hilf, S. R. Davies, A. R. Oseroff, I. Roy, T. Y. Ohulchanskyy, E. J. Bergey, M. R. Detty, *J. Med. Chem.* **2003**, 46, 3734–3747.
- [18] P. J. Chmielewski, L. Latos-Grażyński, M. M. Olmstead, A. L. Balch, *Chem. Eur. J.* **1997**, 3, 268–278.
- [19] M. J. Broadhurst, R. Grigg, A. W. Johnson, *J. Chem. Soc. C* **1971**, 3681–3690.
- [20] a) E. Pacholska-Dudziak, L. Szterenber, L. Latos-Grazynski, *Chem. Eur. J.* **2011**, 17, 3500–3511; b) B. Sathyamoorthy, A. Axelrod, V. Farwell, S. M. Bennett, B. D. Calitree, J. B. Benedict, D. K. Sukumaran, M. R. Detty, *Organometallics* **2010**, 29, 3431–3441; c) M. Abe, M. R. Detty, O. O. Gerlits, D. K. Sukumaran, *Organometallics* **2004**, 23, 4513–4518; d) E. Pacholska, L. Latos-Grazynski, Z. Ciunik, *Angew. Chem.* **2001**, 113, 4598–4601; *Angew. Chem. Int. Ed.* **2001**, 40, 4466–4469; e) L. Latos-Grażyński in *The Porphyrin Handbook*, Vol. 2 (Eds.: K. M. Kadish, K. M. Smith, R. Guilard), Academic Press, New York, **1999**, Chapter 14, pp. 361–416.
- [21] A. Ulman, J. Manassen, *J. Am. Chem. Soc.* **1975**, 97, 6540–6544.
- [22] H. Uno, K. Nakamoto, K. Kuroki, A. Fujimoto, N. Ono, *Chem. Eur. J.* **2007**, 13, 5773–5784.
- [23] Y. Shimizu, Z. Shen, S. Ito, H. Uno, J. Daub, N. Ono, *Tetrahedron Lett.* **2002**, 43, 8485–8488.
- [24] S. Ito, H. Uno, H. Watanabe, T. Murashima, N. Ono, Y. C. Tsai, R. G. Compton, *Tetrahedron Lett.* **2001**, 42, 707–710.
- [25] a) S. Ito, T. Murashima, N. Ono, *J. Chem. Soc. Perkin Trans. 1* **1997**, 3161–3165; b) S. Ito, N. Ochi, T. Murashima, H. Uno, N. Ono, *Heterocycles* **2000**, 52, 399–411; c) T. Okujima, N. Komobuchi, H. Uno, N. Ono, *Heterocycles* **2006**, 67, 255–267.
- [26] a) Y. Shimizu, Z. Shen, T. Okujima, H. Uno, N. Ono, *Chem. Commun.* **2004**, 374–375; b) T. Okujima, N. Komobuchi, Y. Shimizu, H. Uno, N. Ono, *Tetrahedron Lett.* **2004**, 45, 5461–5464.
- [27] J. Mack, M. J. Stillman, N. Kobayashi, *Coord. Chem. Rev.* **2007**, 251, 429–453.
- [28] a) M. Seth, T. Ziegler, A. Banerjee, J. Autschbach, S. J. A. van Gisbergen, E. J. Barends, *J. Chem. Phys.* **2004**, 120, 10942–10954; b) M. Seth, J. Autschbach, T. Ziegler, *J. Chem. Phys.* **2005**, 122, 094112; c) M. Seth, T. Ziegler, *J. Chem. Phys.* **2006**, 124, 144105; d) M. Seth, J. Autschbach, T. Ziegler, *J. Chem. Theory Comput.* **2007**, 3, 434–447; e) M. Krykunov, A. Banerjee, T. Ziegler, J. Autschbach, *J. Chem. Phys.* **2005**, 122, 074105.
- [29] a) G. A. Peralta, M. Seth, T. Ziegler, *Inorg. Chem.* **2007**, 46, 9111–9125; b) G. A. Peralta, M. Seth, H. Zhekova, T. Ziegler, *Inorg. Chem.* **2008**, 47, 4185–4198.
- [30] a) J. Michl, *J. Am. Chem. Soc.* **1978**, 100, 6801–6811; b) J. Michl, *Pure Appl. Chem.* **1980**, 52, 1549–1563; c) J. Michl, *Tetrahedron* **1984**, 40, 3845–3934.
- [31] M. Gouterman in *The Porphyrins*, Vol. III, Part A (Ed.: D. Dolphin), Academic Press, New York, **1978**, pp. 1–165.
- [32] K. M. Kadish, M. M. Morrison, *J. Am. Chem. Soc.* **1976**, 98, 3326–3328.
- [33] Z.-L. Cai, M. J. Crossley, J. R. Reimers, R. Kobayashi, R. D. Amos, *J. Phys. Chem. B* **2006**, 110, 15624–15632.
- [34] As shown by others (see, for example: E. C. A. Ojadi, H. Linschitz, M. Gouterman, R. I. Walter, J. S. Lindsey, R. W. Wagner, P. R. Droupadi, W. Wang, *J. Phys. Chem.* **1993**, 97, 13192–13197) and ourselves (reference [16]) the protonation dynamics of tetra-meso-aniline-substituted porphyrins are rather complex. Because such detailed protonation features are not a focus of this report, we refrained, herein, from a more detailed analysis.

- [35] W. Siebrand, *J. Chem. Phys.* **1967**, *46*, 440–447.
- [36] F. E. Lytle, D. R. Storey, M. E. Juricich, *Spectrochim. Acta A* **1973**, *29*, 1357–1369.
- [37] L. Beverina, A. Abboto, M. Landenna, M. Cerminara, R. Tubino, F. Meinardi, S. Bradamante, G. A. Pagani, *Org. Lett.* **2005**, *7*, 4257–4260.
- [38] S. A. Gerhardt, J. W. Lewis, J. Z. Zhang, R. Bonnett, K. A. McManus, *Photochem. Photobiol. Sci.* **2003**, *2*, 934–938.
- [39] Y. Choi, J. R. McCarthy, R. Weissleder, C. H. Tung, *ChemMedChem* **2006**, *1*, 458–463.
- [40] SMART, SAINT, SADABS, and SHELXTL, Bruker AXS Inc., Madison, **2000**.
- [41] U. Resch-Genger, D. Pfeifer, C. Monte, W. Pilz, A. Hoffmann, M. Spieles, K. Rurack, J. Hollandt, D. Taubert, B. Schönenberger, P. Nording, *J. Fluoresc.* **2005**, *15*, 315–336.
- [42] Y.-H. Yu, A. B. Descalzo, Z. Shen, H. Röhr, Q. Liu, Y.-W. Wang, M. Spieles, Y.-Z. Li, K. Rurack, X.-Z. You, *Chem. Asian J.* **2006**, *1*, 176–187.
- [43] Gaussian 03, Revision C.02, M. J. Frisch, G. W. Trucks, H. B. Schlegel, G. E. Scuseria, M. A. Robb, J. R. Cheeseman, J. A. Montgomery, Jr., T. Vreven, K. N. Kudin, J. C. Burant, J. M. Millam, S. S. Iyengar, J. Tomasi, V. Barone, B. Mennucci, M. Cossi, G. Scalmani, N. Rega, G. A. Petersson, H. Nakatsuji, M. Hada, M. Ehara, K. Toyota, R. Fukuda, J. Hasegawa, M. Ishida, T. Nakajima, Y. Honda, O. Kitao, H. Nakai, M. Klene, X. Li, J. E. Knox, H. P. Hratchian, J. B. Cross, V. Bakken, C. Adamo, J. Jaramillo, R. Gomperts, R. E. Stratmann, O. Yazyev, A. J. Austin, R. Cammi, C. Pomelli, J. W. Ochterski, P. Y. Ayala, K. Morokuma, G. A. Voth, P. Salvador, J. J. Dannenberg, V. G. Zakrzewski, S. Dapprich, A. D. Daniels, M. C. Strain, O. Farkas, D. K. Malick, A. D. Rabuck, K. Raghavachari, J. B. Foresman, J. V. Ortiz, Q. Cui, A. G. Baboul, S. Clifford, J. Ciołowski, B. B. Stefanov, G. Liu, A. Liashenko, P. Piskorz, I. Komaromi, R. L. Martin, D. J. Fox, T. Keith, M. A. Al-Laham, C. Y. Peng, A. Nanayakkara, M. Challacombe, P. M. W. Gill, B. Johnson, W. Chen, M. W. Wong, C. Gonzalez, J. A. Pople, Gaussian, Inc., Wallingford CT, **2004**.
- [44] D. Pez, I. Leal, I. H. Gilberta, *Bioorg. Med. Chem.* **2003**, *11*, 4693–4711.
- [45] B. H. Novak, T. D. Lash, *J. Org. Chem.* **1998**, *63*, 3998–4010.
- [46] A. Ulman, J. Manassen, *Tetrahedron Lett.* **1978**, *19*, 167.
- [47] A. S. Hay, *J. Org. Chem.* **1962**, *27*, 3320.
- [48] C. Hansch, A. Leo, R. W. Taft, *Chem. Rev.* **1991**, *91*, 165–195.

Received: March 21, 2012

Revised: August 3, 2012

Published online: November 13, 2012